One-pot conversion of lignocellulosic biomass to ketones and aromatics over a multifunctional Cu–Ru/ZSM-5 catalyst

Gladys Tiffany Jaya [a,1], Rizki Insyani [b,1], Jaeyong Park [a], Amsalia Florence Barus [b],
Malayil Gopalan Sibi [a,b,c], Virendra Ranaware [b], Deepak Verma [a,b,c,*], Jaehoon Kim [a,b,c,*]

[a] School of Mechanical Engineering, Sungkyunkwan University, 2066 Seobu-Ro, Jangan-Gu, Suwon, Gyeonggi-Do 16419, Republic of Korea
[b] SKKU Advanced Institute of Nanotechnology (SAINT), Sungkyunkwan University, 2066 Seobu-Ro, Jangan-Gu, Suwon, Gyeonggi-Do 16419, Republic of Korea
[c] School of Chemical Engineering, Sungkyunkwan University, 2066 Seobu-Ro, Jangan-Gu, Suwon, Gyeonggi-Do 16419, Republic of Korea

ARTICLE INFO

ABSTRACT

The complete conversion of lignocellulosic biomass to selective and highly valuable chemicals is challenging because of its inertness and complexity. Herein, we report a direct chemocatalytic route for the complete one-pot conversion of raw woody biomass to cyclic ketones and aromatic monomers over a multifunctional bi-metallic Cu–Ru catalyst on HZSM-5 (Cu–Ru/Z). The Si/Al ratio of HZSM-5 plays an effective role in the product distribution. High-yield ketones (60.9% based on carbon in holocellulose) and aromatics (28.4% based on carbon in lignin) were produced in an aqueous medium. Three strategies, metal domain encapsulation inside the zeolitic framework, SiO_2 layer coating, and carbon layer coating, were employed to overcome the weak hydrothermal stability associated with HZSM-5. The carbon-coated Cu–Ru/Z catalyst exhibited high stability up to three reaction cycles. Optimization of the reaction conditions, reaction mechanisms for the selective ketone synthesis, and catalyst deactivation mechanisms are discussed.

1. Introduction

Because of concerns related to global warming due to the extensive use of fossil fuels, renewable resources in the energy and chemical sectors are essential alternatives for establishing a sustainable society [1]. Wind and solar power are the two main renewable energy sources, and the current trend for electrification can reduce the extensive use of liquid fuels in the transportation sector. However, producing renewable platform chemicals that are widely used in various chemical industries remains challenging. Lignocellulosic biomass, which comprises cellulose (40–50 wt%), hemicellulose (16–33 wt%), and lignin (15–30 wt%) [1], is considered one of the most promising and economically feasible resources for producing renewable chemicals. Despite wide availability, global distribution, and low cost, the complex structure, robustness, and resistance to chemical transformation of lignocellulosic biomass make it difficult to selectively convert it to desired platform chemicals.

Most contemporary lignocellulosic biomass conversion approaches comprise several consecutive unit conversion and separation processes.

For example, to produce 2,5-dimethylfuran (2,5-DMF), a promising fuel additive [2], lignocellulosic biomass fractionation, cellulose-to-glucose hydrolysis, glucose-to-fructose isomerization, fructose-to-5-hydroxymethylfurfural (5-HMF) dehydration, and subsequent 5-HMF hydrogenolysis and hydrogenation are required [3,4]. In addition, to achieve highly selective targeted chemicals, the separation and purification of the reaction mixture produced at each step should be carefully considered, which makes the process tedious, time- and energy-consuming, and expensive. Some thermochemical conversion techniques, such as pyrolysis and liquefaction, can realize the one-pot conversion of lignocellulosic biomass to bio-oil; however, the product comprises highly oxygenated and unselective chemicals, which should be upgraded for use in the transportation sector [5,6]. Therefore, it is highly desirable to develop a promising route for the complete one-pot, chemocatalytic conversion of biomass to selective chemicals.

Because one-pot conversion of lignocellulosic biomass to selective chemicals requires several consecutive reactions, such as hydrolysis, isomerization, and hydrogenation, it is desirable to realize the complete

biomass conversion over multifunctional catalysts in an appropriate medium [7–9]. Studies on direct lignocellulosic biomass conversion have focused on the production of gasoline-fraction fuels (e.g., C_5–C_6 n-alkanes and branched alkanes [10–12] and substituted cycloalkanes [10]), commodity chemicals (e.g., diols [13] and alcohols [10,14]), and phenolic derivatives [10,13], as listed in Table S1. Li et al. [13] reported the almost complete conversion of birchwood over a Ni–W_2C/AC catalyst to diols (e.g., ethylene glycol, 1,2-propylene glycol, and 1, 2-butylene glycol) at a yield of 70.6 wt% based on the holocellulose content and phenolic monomers at a yield of 36.9 wt% based on the lignin content under H_2 at 235 °C and 6 MPa for 4 h. When pinewood was used as a feedstock, the diol and phenolic monomer yield decreased to 43.5 and 10.1 wt%, respectively. Liu et al. [10] reported three catalytic systems to convert raw biomass to cyclic/non-cyclic alkanes and lignin-derived phenolic monomers (LDPMs). Over layered $LiTaMoO_6$ and Ru/C in an aqueous phosphoric acid medium, 82.4 C% gasoline and 35.7 C% phenolic derivatives were achieved from corn stalk under H_2 at 230 °C and 6 MPa for 24 h. Xia et al. [12] reported direct birchwood deoxygenation to n-alkanes and cycloalkanes over $Pt/NbOPO_4$ under H_2 at 190 °C and 5 MPa for 20 h in cyclohexane with a total liquid alkane yield of 24.9 wt%. In some studies, the production of LDPMs during the complete biomass conversion [10] results from the dissociation of C–O bonds in native lignin under some selective media (e.g., methanol and water) and subsequent monomer catalytic stabilization [15–17]. Although great success has been achieved for the direct conversion of lignocellulosic biomass to gasoline fractions and diols, it is highly desirable to develop a technique that can synthesize value-added fine chemicals for realizing economically feasible wood-based biorefineries.

Among potential chemicals that can be synthesized from carbohydrates, cyclic ketones, such as cyclopentanone (CPO) and its methyl derivatives (mCPOs), are considered highly valuable chemicals, which can be used to produce pesticides, fungicides, pharmaceuticals, solvents for electronics, and rubbers. As shown in Fig. S1, the fossil-based route for commercial CPO production is the decarboxylative ketonization of adipic acid in the presence of $Ba(OH)_2$ at high temperatures (285–295 °C) [18,19]. In 2020, the CPO global market value was approximately 1.9 billion USD, which is estimated to increase at a 8.66% rate by 2027 [20]. In addition, CPO derivatives, such as 2-methyl cyclopentanone (2-mCPO) and 3-methyl cyclopentanone (3-mCPO) and their respective olefins, i.e., 2-methyl-2-cyclopenten-1-one (2-mCPeO) and 3-methyl-2-cyclopenten-1-one (3-mCPeO), are valuable intermediates to produce important drug molecules (e.g., MK-0354 [21] and falcipain inhibitors [22]) and high-density rocket fuels [23]. Previous studies have demonstrated that CPO and mCPOs could be synthesized from holocellulose-derived 6- and 5-membered cyclic aldehydes such as 5-hydroxymethylfurfural (5-HMF) and furfural (FFA) via consecutive hydrogenation (HD) and hydrodeoxygenation (HDO) routes (Fig. S1) [24–27]. The HDO and subsequent HD of 5-HMF produces 2,5-DMF; 2,5-DMF further undergoes ring opening to produce 2, 5-hexadione (2,5-HDN), and then 2,5-HDN cyclization via intramolecular aldol condensation produces 3-mCPeO and subsequently 3-mCPO via HD. Whereas FFA-to-CPO production involves two steps, selective FFA-to- furfuryl alcohol (FOL) and FOL-to-CPO HD is realized through a furan ring opening-electrocyclization process, which is also known as Piancatelli rearrangement [28,29]. In this rearrangement, 4-hydroxy-2-cyclopentenone (HCP) as an intermediate is produced from FOL via ring opening and closure, which could further selectively hydrogenate to CPO. However, direct conversion of raw lignocellulosic biomass to CPO and its derivatives has not been explored yet.

In this study, we report the design of a multifunctional HZSM-5-supported bi-metallic Cu–Ru catalyst for the one-pot direct conversion of raw lignocellulosic biomass to commodity chemicals in an aqueous medium. To the best of our knowledge, CPO production, or that of its methyl derivatives, from raw biomass or its derived mono-, di-, or polysaccharides has not been reported to date. Interestingly, during the course of this study, no chemically pre-treated biomass was used as

feedstock. An activated reductive deposition (ARD) method was used to synthesize the bi-metallic Cu–Ru on HZSM-5 catalyst. Furthermore, during the repeated runs, catalyst stability under hydrothermal conditions was also investigated, which was directly affecting the product yield. Therefore, to stabilize the zeolite framework and catalyst activity under hydrothermal conditions, an alternative approach was applied in which Cu–Ru nanoparticle (NP) encapsulation and zeolite crystal coating by amorphous SiO_2 and carbon were used. Based on the catalytic activity results, a reasonable reaction mechanism was proposed and proven through controlled experiments.

2. Experimental

2.1. Materials

Ammonium-form ZSM-5 (NH$_4$–ZSM5) with Si/Al ratios of 12.5, 40, and 100, ruthenium(III) chloride (RuCl$_3$, ≥99.5%), copper(II) nitrate hemi(pentahydrate) (Cu(NO$_3$)$_2$·2.5 H$_2$O, ≥ 99.9%), hydrazine monohydrate (N$_2$H$_4$·H$_2$O, >98%), cellobiose (≥98%), *d*-fructose (99%), cyclopentanone (CPO, 99%), furfural (FFA, >98%), polyvinylpyrrolidone (PVP, average molecular weight (M$_w$) = 10,000 g mol^{-1}), n-dodecane (C$_{12}$H$_{26}$, ≥99%), and ammonium nitrate (NH$_4$NO$_3$, 98%) were purchased from Thermo Fisher Scientific (USA). Palladium chloride (PdCl$_2$, >99%), sulfuric acid (H$_2$SO$_4$, 98%), sodium hydroxide (NaOH, ≥97.0%, pellets), *d*-glucose (>99%), cellulose (microcrystalline powder), tetraethyl orthosilicate (TEOS, 98%), aluminum isopropoxide (AIP, ≥98%), ethylene glycol (EG, 99.8%), silicon dioxide (SiO$_2$ nanopowder with a particle size of 5–15 nm, 99.5% trace metal basis), anatase titanium (IV) oxide (TiO$_2$, ≥99% trace metal basis, powder), dodecyltrimethylammonium bromide (DDAB, >98%), formaldehyde (37 wt% in H$_2$O), and 4-*n*-propyl guaiacol were purchased from Sigma–Aldrich (USA). High-performance liquid chromatography (HPLC) grade water, ethanol, acetone, methanol, dichloromethane (DCM), and hydrochloric acid (HCl, 35%) were purchased from Daejung Chemical (South Korea). Tetrapropylammonium hydroxide (TPAOH, 20–25% in water) was purchased from Tokyo Chemical Industry (Japan). Niobium (V) oxide (Nb$_2$O$_5$) was purchased from Junsei Chemical Co., Ltd. (Japan). All chemicals were used as received without further purification. Distilled and deionized (DDI) water was produced using an EXL® 7 S Analysis water purification system equipped with a 0.22-μm filter (Vivagen Co., Ltd., South Korea). Oakwood (*Quercus sp.*, hardwood), pinewood (*Pinus sp.*, softwood), birchwood (*Betula sp.*, hardwood) and silvergrass (*Miscanthus sp.*, grass) were acquired from a local market in South Korea. The constituents of the biomass are listed in Table S2.

2.2. Catalyst preparation

2.2.1. Mono- (Cu or Ru) and bi-metallic Cu–Ru/HZSM-5 catalyst preparation

The NH$_4$–ZSM-5 was activated in a calcination tube under an air flow at 50 mL min^{-1} at 450 °C for 3 h to obtain HZSM-5. The ARD method was used to impregnate the Cu and Ru metal NPs on the HZSM-5 support. In the synthesis of mono- and bi-metallic Ru–Cu catalysts, 1 g of HZSM-5 was introduced into 30 mL methanol solution of RuCl$_3$ and Cu (NO$_3$)$_2$•2.5H$_2$O with desired concentrations, then the dispersion was stirred for 6 h. While stirring, 2 mL of N$_2$H$_4$•H$_2$O in methanol at a concentration of 0.1 v/v% was added dropwise to the HZSM-5 suspension in the RuCl$_3$ and Cu (NO$_3$)$_2$•2.5H$_2$O solution. Then, the mixture was continuously stirred for 6 h at 25 ± 2 °C. Subsequently, the produced solid was washed with methanol, collected via centrifugation, and dried overnight in a convection oven at 80 °C. The solid powder was further reduced under a H$_2$/Ar flow at 50 mL min^{-1} at 500 °C for 5 h. The produced bi-metallic catalysts were denoted as *x*C–*y*R/Z(*z*), where *x* is the Cu loading, *y* is the Ru loading, *z* is the Si/Al ratio, C is Cu, R is Ru, and Z is HZSM-5. For comparison purposes, mono-metallic Cu or Ru was loaded on the HZSM-5 using the same procedure as that used for the

synthesis of the bi-metallic C–R/Z catalysts. The mono-metallic catalysts were denoted as xC/Z(z) and yR/Z(z) according to the use of Cu or Ru, respectively. In addition, to examine the role of the support, bi-metallic Cu–Ru NPs were loaded on SiO_2, TiO_2, and Nb_2O_5 supports using the same procedure as that used for the synthesis of the bi-metallic Cu–Ru/Z catalysts.

2.2.2. Encapsulated xCu–yRu/HZSM-5 catalyst preparation

Solution A was prepared by dissolving 21.13 g of TEOS, 20.3 g of TPAOH, and 0.14 g of AIP (Si/Al ratio of approximately 140) in 12 mL DDI water while stirring for 24 h at 25 ± 2 °C. Separately, solution B was prepared by dissolving 0.09 g of $RuCl_3$, 0.19 g of $Cu(NO_3)_2 \cdot 2.5\,H_2O$, and 0.25 g of PVP in 80 mL ethylene glycol under ultrasonication treatment to obtain a homogeneous precursor solution. Afterwards, solution B was transferred into a 250 mL two-neck round-bottom flask and then refluxed at 200 °C for 15 min under a N_2 atmosphere to synthesize Ru–Cu NPs. After the temperature decreased to 25 ± 2 °C, the refluxed solution was washed with acetone and centrifuged to collect the Ru–Cu NPs. Then, the Ru–Cu NPs were dispersed in 5 mL DDI water and sonicated to ensure a homogeneous dispersion. Subsequently, solution A was added to the Ru–Cu NP dispersion. The entire mixture was transferred to a Teflon-lined stainless-steel reactor with an inner volume of 100 mL and kept at 200 °C for 3 days. The produced solid was collected via filtration and calcined in air at 450 °C for 3 h. The calcined sample was then reduced under a H_2/Ar flow at 50 mL min^{-1} at 450 °C for 5 h. The synthesized catalysts were denoted as xC–yR/Z$_s$(z)-E, where subscript s indicates synthesis and E indicates encapsulation.

2.2.3. Synthesis of HZSM-5(100)

HZSM-5$_s$(100), denoted as Z$_s$(100), was synthesized employing a hydrothermal method. In the synthesis, a solution mixture was prepared by adding 20.3 g of TPAOH and 0.13 g of AIP to 10 mL of DDI water, and the mixture was continuously stirred at 25 ± 2 °C for 2 h to produce a clear solution. Then, 21.1 g of TEOS was added to the aqueous TPAOH and AIP solution, and the entire mixture was left stirring for an additional 4 h to produce a clear solution. Then, the solution was transferred to a Teflon-lined stainless-steel reactor with an inner volume of 100 mL and kept at 200 °C for 3 days. The produced white solid was recovered via filtration and dried overnight in a convection oven at 80 °C. The synthesized Z$_s$(100) was calcined at 550 °C for 4 h prior to metal loading.

2.2.4. Bi-metallic 5C–5R/Z$_s$(100) catalyst preparation

The ARD procedure detailed in Section 2.2.1 was used to synthesize the 5C–5R/Z$_s$(100) catalyst.

2.2.5. SiO₂- and C-coated bi-metallic 5Cu–5Ru/HZSM-5(100)$_s$ catalyst preparation

A modified Stöber method [30] was used to coat the external surface and pore mouth of 5C–5R/Z$_s$(100) catalysts with a SiO_2 layer. In the coating procedure, 0.5 g of the as-synthesized 5C–5R/Z$_s$(100) catalyst was dispersed in 150 mL of ethanol via sonication and 1.0 mL of TEOS was added to the dispersion under stirring for 30 min. Then, 10 mL NH_4OH was added dropwise into the dispersion and the final mixture was continually stirred for 4 h at 25 ± 2 °C. Finally, the synthesized sample was collected via filtration and dried overnight in a convection oven at 80 °C. The dried sample was calcined at 550 °C for 4 h in an air flow at 100 mL min^{-1} and subsequently reduced under a 5% H_2/Ar flow at 50 mL min^{-1} at 450 °C for 4 h. The synthesized catalyst was denoted as 5C–5R/Z$_s$(100)@SiO_2. A resorcinol-formaldehyde resin (RF) polymer coating using a sol-gel method followed by carbonization was used the carbon coating [31]. In this procedure, 0.5 g of 5C–5R/Z$_s$(100) catalyst and 0.1 g of DDAB were added to 35 mL DDI water, the mixture was continuously sonicated for 30 min. Afterwards, 10.5 mL ethanol, 0.15 g resorcinol, and 0.1 mL NH_4OH were added to the dispersion and stirred at 35 °C for 30 min. Finally, 0.4 mL of formaldehyde was added

dropwise into the solution and left under continuous stirring at 35 °C for 6 h and then aged at 25 ± 2 °C for 12 h. The RF-coated 5C–5R/Z$_s$(100) catalyst was collected via centrifugation and washed with ethanol followed by water to remove the DDAB template and unreacted phenolic species. Then, the washed sample was dried overnight in a convection oven at 80 °C and calcined at 550 °C for 5 h under a N_2 flow at 100 mL min^{-1}. The synthesized catalyst was denoted as 5C–5R/Z$_s$(100)@C.

2.3. Catalyst characterization

The textural properties of the catalysts were examined by collecting N_2 adsorption–desorption isotherms at −196 °C using a Belsorp-mini II apparatus (BEL Inc., Japan). Prior to performing the measurements, all samples were degassed in a vacuum at 120 °C for 8 h using a BEL-PREP–vac II apparatus (BEL Inc.) to remove any absorbed moisture and other light species. The specific surface area and pore size distribution were calculated using the Brunauer–Emmett–Teller (BET) and Barrett–Joyner–Halenda (BJH) methods, respectively. The crystalline structure of the catalysts was measured using a D8 Advance X-ray diffractometer (XRD, Bruker Corporation, USA) equipped with a LynxEye detector coupled to an X-ray generator tube at Cu-Kα ($\lambda = 1.5418$ Å) and nickel foil-K$_\beta$ filtered radiation at 20 mA and 40 kV. The XRD patterns were recorded at 2θ values in the range 3–90° with a scanning speed of 5 ° min^{-1}. X-ray photoelectron spectroscopy (XPS) measurements were performed in an ESCALAB 250Xi (Thermo Scientific, UK) twin-crystal micro-focusing X-ray monochromator using Al-Kα anode radiation as the excitation source. X-ray absorption spectroscopy (XAS) experiments were carried out employing a synchrotron radiation light source at the 8 C beamline of the Pohang Accelerator Laboratory using a Si(111) double-crystal monochromator. For energy calibration, the reference spectra of metal foils (Cu and Ru) and their respective possible oxides in powder form (CuO, Cu_2O, and RuO_2) were obtained simultaneously. The catalyst samples were measured at both the Ru-K and Cu-K X-ray absorption edges at 25 ± 2 °C. X-ray absorption near-edge spectroscopy (XANES) and extended X-ray absorption fine structure (EXAFS) data were processed using the Athena/Artemis software package. The extracted EXAFS signal, $\chi(k)$, was weighted by k^3 to clarify the high-energy oscillations. Fourier-transform was performed in the k-range of 3.0–11.0 Å using a Hanning window function to produce the magnitude plot of the EXAFS spectra in the R-space.

The Cu and Ru metal contents in the catalysts were quantified using inductively coupled plasma-optical emission spectroscopy (ICP–OES, Varian Model 730-ES, USA). High-resolution transmission electron microscopy (HR–TEM) images were obtained using a JEM-ARM200F (JEOL, Japan) spherical aberration-corrected field-emission transmission electron microscope operated at an accelerating voltage of 200 kV. In addition, the morphology of the catalysts was observed using a high-angle annular dark-field scanning TEM (HAADF−STEM; JEM-3010, JEOL, Japan) device with an electron acceleration energy and spatial resolution of 300 keV and 1.4 Å, respectively. Field-emission scanning electron microscopy (FE–SEM) images were taken using a JSM7000F (JEOL, Japan) device equipped with an energy dispersive X-ray spectrometer (EDS).

To investigate the thermal behavior of the catalysts and coke formation, thermogravimetric analyses (TGAs) were carried out using a Q50 thermogravimetric analyzer (TA Instruments, USA) from 30° to 800°C at a heating and air flow rate of 10 °C min^{-1} and 60 mL min^{-1}, respectively. CO and N_2O chemisorption were performed using a BELCAT-M instrument (BET Inc., Japan) equipped with a thermal conductivity detector (TCD). Prior to the pulse chemisorption analyses, each catalyst sample was reduced at 450 °C for 2 h under a 5% H_2/Ar (99.999%, JC Gas Company, South Korea) flow at 30 mL min^{-1}. Then, the sample tube was naturally cooled to 50 °C. Subsequently, the sample was flush with He gas (99.999%, JC Gas Company) at a flow rate of 30 mL min^{-1} at 50 °C for 30 min to remove physically adsorbed H_2 molecules. Then, a CO (4.97% CO/He, 99.999%, JC Gas Company) or N_2O

(5% N_2O/He, 99.999%, JC Gas Company) pulse was injected to a sample loop with an inner volume of 0.988 mL. For the CO-pulsed chemisorption measurements, CO gas was flowed for at least 10 min into the charging sample loop prior to being injected to the sample tube. The pulse measurement was repeated until the peak reached its saturation point. In the N_2O chemisorption case, N_2O was injected by a pulse, and the N_2O decomposition was monitored by placing a Porapak N column between the sample tube and the TCD to separate N_2 and residual N_2O. The dispersion of copper metal (D_{Cu}) was calculated via dissociative N_2O chemisorption using Eqs. (1) and (2). A surface density of 1.46×10^{19} atoms per m^2 for Cu [32] was used for the D_{Cu} measurements.

$$2Cu + N_2O \rightarrow Cu_2O + \quad N_2 \tag{1}$$

$$D_{Cu} = \frac{2 \quad \times \quad N_2O \text{ chemisorbed}}{No. of \text{ Cu atoms}} \tag{2}$$

Hydrogen temperature-programmed reduction (H_2–TPR) analyses were performed to assess the reducibility of metal sites in the catalysts using the BELCAT-M instrument. A known amount of catalyst (0.05 g) was added to the quartz sample tube. Prior to H_2 adsorption, the sample tube was heated to 150 °C at a heating rate of 10 °C min^{-1} under an ultrahigh-purity Ar gas (99.999%, JC Gas Company) flow rate of 30 mL min^{-1}. The sample tube temperature was maintained at 150 °C for 1 h to remove any adsorbed water or volatile species from the catalyst surface. Then, the catalyst was oxidized under an O_2 gas (99.995%, JC Gas Company) flow at a rate of 30 mL min^{-1} at 400 °C for 2 h. The sample tube was then naturally cooled to 50 °C, flushed with Ar for 30 min, and saturated with a 5% H_2/Ar flow at 50 mL min^{-1} for 1 h. Then, the temperature of the sample tube was increased to 800 °C at a heating rate of 10 °C min^{-1} under a 5% H_2/Ar flow at 30 mL min^{-1} for the H_2–TPR analysis. The total H_2 consumption was monitored using the TCD and recorded as a function of temperature.

The hydrogen temperature-programmed desorption (H_2–TPD) was performed using the BELCAT-M instrument. A catalyst aliquot (0.05 g) was added to the quartz sample tube. Before H_2 adsorption, the sample was reduced at 450 °C under a heating rate of 5 °C min^{-1} under an ultrahigh-purity 5% H_2/Ar gas (99.999%) flow at a rate of 30 mL min^{-1} for 2 h. Then, the sample tube was naturally cooled to 50 °C and the catalyst was saturated under a 5% H_2/Ar flow at a rate of 30 mL min^{-1} for 1 h. Ultrahigh-purity Ar gas (99.999%) was used to flush the entire system at a flow rate of 30 mL min^{-1} at 50 °C for 30 min to remove physically adsorbed H_2 molecules. Next, the temperature of the sample tube was increased to 800 °C at a heating rate of 10 °C min^{-1} and under an ultrahigh-purity Ar gas flow at a rate of 30 mL min^{-1} for the H_2–TPD analysis. The total acidity of the catalysts was measured via ammonia temperature-programmed desorption (NH_3–TPD). Prior to the NH_3–TPD measurements, each catalyst (0.05 g) was heat-treated at 200 °C for 1.5 h under a He flow rate of 30 mL min^{-1}. Upon cooling to 50 °C, the samples were saturated with NH_3 under a 4.98% NH_3/He (99.995%, JC Gas Company) flow at a rate of 30 mL min^{-1} for 30 min followed by

and a Praying Mantis (Harrick, USA) cell. A uniform KBr and catalyst sample mixture (95:5 wt ratio) was prepared by mortar mixing and loaded into the DRIFT cell. Then the cell temperature was increased to 150 °C at a heating rate of 10 °C min^{-1} under a high-purity N_2 (99.999%) flow at a rate of 50 mL min^{-1} for 2 h, followed by reduction at 450 °C at a heating rate of 10 °C min^{-1} under a H_2 (99.999%) flow at a rate of 50 mL min^{-1} for 3 h. After cooling to 50 °C, the DRIFT cell was flushed with N_2 at a flow rate of 50 mL min^{-1} for 1 h, and the background spectra were collected. The catalyst mixture sample was subsequently exposed to a pyridine flow by purging the glassware containing pyridine with N_2 at a flow rate of 50 mL min^{-1} at 50 °C for 1 h. Next, the catalyst mixture sample was flushed with N_2 at a flow rate of 10 mL min^{-1} for 30 h and the DRIFT cell was kept in a vacuum for 1 h to remove physiosorbed pyridine species. The DRIFT spectra were recorded at 30 ± 2 °C.

2.4. Catalytic activity

Direct conversion of lignocellulose biomass (oakwood, birchwood, silvergrass, and pinewood), cellulose, *d*-glucose, *d*-fructose, and xylose was carried out in a custom-built stainless steel 316 batch reactor with an inner volume of 140 mL and equipped with a mechanically driven agitator, thermocouples, and gas lines. A detailed description of the reactor system can be found in [33]. In a typical reaction, the catalyst and feed (1:2 wt ratio) were added to the reactor along with 30 mL water. Then, the reactor was tightly sealed and purged with H_2 gas for 3 min using a deep purge line to remove dissolved O_2 and O_2 from the reactor head. The reactor was then pressurized with H_2 to 1.0–4.0 MPa and then heated to specific temperatures between 260 and 320 °C at a heating rate of approximately 10 °C min^{-1}, and the reaction was maintained for durations between 0.5 and 6 h at a stirring rate of 500 rpm. When the reactions were completed, they were stopped by quickly cooling the reactor using an ice water bath followed by depressurization to atmospheric pressure. After the reactor was opened, 30 mL DCM was added to the reaction mixture. The catalyst and the solid residue in the reaction mixture were subsequently separated from liquid products via filtration. After 1 mL DCM phase was taken from the reaction mixture, 1 μL *n*-dodecane as an internal standard was added to the DCM phase for the qualification and quantification analyses. Thereafter, the reaction mixture was collected in a beaker by washing the reactor with water and DCM to dissolve the decomposed holocellulose- and lignin-derived components. The liquid and solid mixture was separated using a polyvinylidene difluoride (PVDF, Whatman, USA) filter with a pore size of 0.45 μm, and the solid product was washed with DDI water and DCM to dissolve soluble organics and transfer to the filtrate phase. Then, the remaining solid residue and the catalyst were washed with acetone to recover acetone-soluble products (ASPs). The solid residue and the catalyst were then dried overnight in a vacuum oven at 80 °C to calculate the feed conversion according to Eq. (3).

$$\text{Feed conversion}(\%) = \left(1 - \frac{\text{weight of (solid residue + catalyst)} - \text{weight of catalyst}}{\text{weight of initial biomass}}\right) \times 100\% \tag{3}$$

flushing with a He flow at a rate of 30 mL min^{-1} for 30 min. NH_3 desorption was performed by increasing the temperature from 50° to 800°C at a heating rate of 10 °C min^{-1} under a He flow rate of 30 mL min^{-1}.

To analyze the nature and strength of the acid sites, the pyridine-adsorbed diffuse reflectance infrared Fourier-transform (py–DRIFT) spectra of the catalysts were collected using a Frontier (PerkinElmer, USA) spectrometer equipped with a mercury cadmium telluride detector

Liquid–liquid extraction (LLE) of the filtrate was conducted in a separatory funnel to separate DCM-soluble products (DSPs) and water-soluble products (WSPs). The separation procedure is shown in Fig. S2.

2.5. Product analysis

The DSPs were analyzed via gas chromatography–time-of-flight mass

Table 1
Physicochemical properties of the zeolite supports, mono-metallic Ru and Cu catalysts, and bi-metallic xCu–yRu/Z(z) catalysts.

Catalyst	Metal loading[a] (wt%)		Textural properties[b]			Metal dispersion	
	Theoretical Cu/Ru	Experimental Cu/Ru	S_{BET}[c] (m^2 g^{-1})	P_v[d] (cm^3 g^{-1})	D_p[e] (nm)	Cu[f]	Ru[g]
Z(12.5)	N.A.[h]	N.A.	420	0.23	2.39	N.A.	N.A.
Z(40)	N.A.	N.A.	458	0.26	2.28	N.A.	N.A.
Z(100)	N.A.	N.A.	408	0.22	2.38	N.A.	N.A.
Z$_s$(100)	N.A.	N.A.	409	0.24	2.23	N.A.	N.A.
5C/Z(100)	5/0	4.7/0	349	0.23	2.53	6.3	N.A.
5R/Z(100)	0/5	0/4.3	352	0.23	2.58	N.A.	8.13
5C–1R/Z(100)	5/1	N.A.	398	0.22	2.77	5.8	1.01
5C–3R/Z(100)	5/3	5.3/2.80	374	0.21	2.25	6.7	2.09
5C–5R/Z(100)	5/5	5.1/4.75	341	0.21	2.51	7.6	4.34
5C–5R/Z(40)	5/5	N.A.	386	0.24	2.50	8.8	4.21
5C–5R/Z(12.5)	5/5	N.A.	365	0.20	2.29	N.A.	4.52
5C–5R/Z(100)-S[i]	5/5	3.4/3.7	210	0.22	2.15	6.0	3.13
5C–5R/Z(100)-E	5/5	2.3/1.8	411	0.25	2.22	8.3	5.22
5C–5 R/Z$_s$(100) @SiO$_2$	N.A.	N.A.	467	0.29	2.29	N.A.	6.11
5C–5R/Z$_s$(100) @C	N.A.	N.A.	532	0.26	2.25	N.A.	7.74
5C–5R/Z$_s$(100) @C-S[j]	N.A.	N.A.	449	0.32	3.06	N.A.	7.59

[a] Determined via ICP–OES.
[b] Determined using N$_2$ adsorption–desorption isotherms.
[c] S_{BET}: Brunauer–Emmett–Teller surface area.
[d] P_v: pore volume.
[e] D_p: mean pore diameter that was determined at P/P$^\circ$ = 0.990.
[f] Determined via dissociative N$_2$O chemisorption.
[g] Determined via CO chemisorption.
[h] N.A.: not available
[i] After the 1st run, the spent catalyst was washed with water and acetone followed by drying at 80 °C. Then, the dried catalyst was calcined at 550 °C in air followed by activation at 450 °C for 4 h in a H$_2$/Ar flow.
[j] After the 3rd run.

spectrometry (GC–TOF/MS). An Agilent 7890 N GC (Agilent Technologies, USA) and a Pegasus high-throughput (HT) TOF/MS system (Leco Corporation, USA) were equipped with an auto injector (Agilent 7860 N) and an Rxi-5Sil-MS column (30 m × 0.25 μm, inner diameter = 0.25 mm, Restek, USA). Ultra-high-purity He (99.9999%) at a flow rate of 1.0 mL min^{-1} was used as the carrier gas. Typically, 1 μL of the sample was injected into the column with a 5:1 split ratio. The injector temperature was set at 250 °C and the transfer line temperature was fixed at 260 °C. The column temperature was programmed to start heating from 40° to 300°C with a heating rate of 10 °C min^{-1}. The detectable mass range for the MS was set at 35–650 m/z. The quantitative analyses of the DSPs were carried out in an Agilent 6890 N GC equipped with a flame ionization detector (FID) and an Rxi-5Sil-MS capillary column (30 m × 0.25 μm, inner diameter = 0.25 mm, Restek). An injection volume of 1 μL with a 10:1 split ratio was used for the measurements. The temperature of the injector inlet and detector was set at 250 °C. The initial column temperature was 40 °C, which was then increased to 250 °C at a heating rate of 10 °C min^{-1}. All product yields were calculated via the effective carbon number method [15,34] using n-dodecane as the internal standard according to Eqs. (4)–(6).

$$\text{Weight of product}(m_{product}) = m_{internal\ std} \times \frac{Area_{product}}{Area_{internal\ std}} \times \frac{ECN_{internal\ std}}{ECN_{product}} \quad (4)$$

$$\text{Mass of Carbon}_{monomer} = n_{monomer} \times \Sigma Carbon_{monomer} \times MW_{monomer} \quad (5)$$

$$\text{Yield}_{monomer} = \frac{\text{mass of Carbon}_{monomer}}{\text{mass of Carbon}_{holocellulose}} \times 100\% \quad (6)$$

Carbon balance was calculated based on the identified compounds using GC–TOF/MS, GC–FID and HPLC.

The WSPs were analyzed via HPLC, which was performed using a Waters Alliance e2695 equipped with a refractive index (RI) detector. A Bio-Rad Aminex HPX-87 H Ion Exclusion (300 × 7.8 mm) column was used along with 0.13 N H$_2$SO$_4$ as mobile phase at 0.65 mL min^{-1} and 50 °C to separate the compounds. The molecular weights of the WSPs were measured via gel-filtration chromatography (GFC) using an Agilent 1100 series HPLC apparatus equipped with a TSKgel G5000PW$_{XL}$ column (TOSOH, Japan; internal diameter: 7.8 mm; length: 300 mm) and an RI detector. The mobile phase flow rate was set at 1 mL min^{-1}. Polyethylene glycol (1.06–21.16 Da) and polyethylene oxide (19.52–1039 kDa) standards, which were purchased from Agilent (USA), were used to calibrate the column. The composition of the gaseous products was analyzed using a PerkinElmer Clarus 600 GC-Model Arnel 1115PPC Refinery Gas Analyzer (RGA-GC, PerkinElmer, CT, USA). Details regarding the specifications of this instrument have been previously reported elsewhere [35].

The ASPs were analyzed via matrix-assisted laser desorption/ionization–time-of-flight mass spectroscopy (MALDI–TOF/MS) to identify the molecular weights of the products using an UltrafleXtreme (Bruker Corp., USA) apparatus at an accelerating voltage of 20 kV. A 200-Hz pulsed Nd:YAG laser (355 nm) was used and positive ion MALDI–TOF/MS profiles were collected from the average signal of 1500 laser shots in linear detection mode. The matrix used for sample analysis was 2,5-dihydroxyl benzoic acid (DHB, Sigma–Aldrich) dissolved in an acetonitrile–water–trifluroacetic acid mixture (666:333:1) with a concentration of 25.0 mg mL^{-1}.

$$\text{Carbon balance}(\%) = \frac{\sum (\text{moles of detected molecules(mol)} \times \text{number of carbon atoms in the product molecule})}{\text{moles of initial substrate(mol)} \times \text{number of carbon atoms in initial substrate}} \times 100\% \quad (7)$$
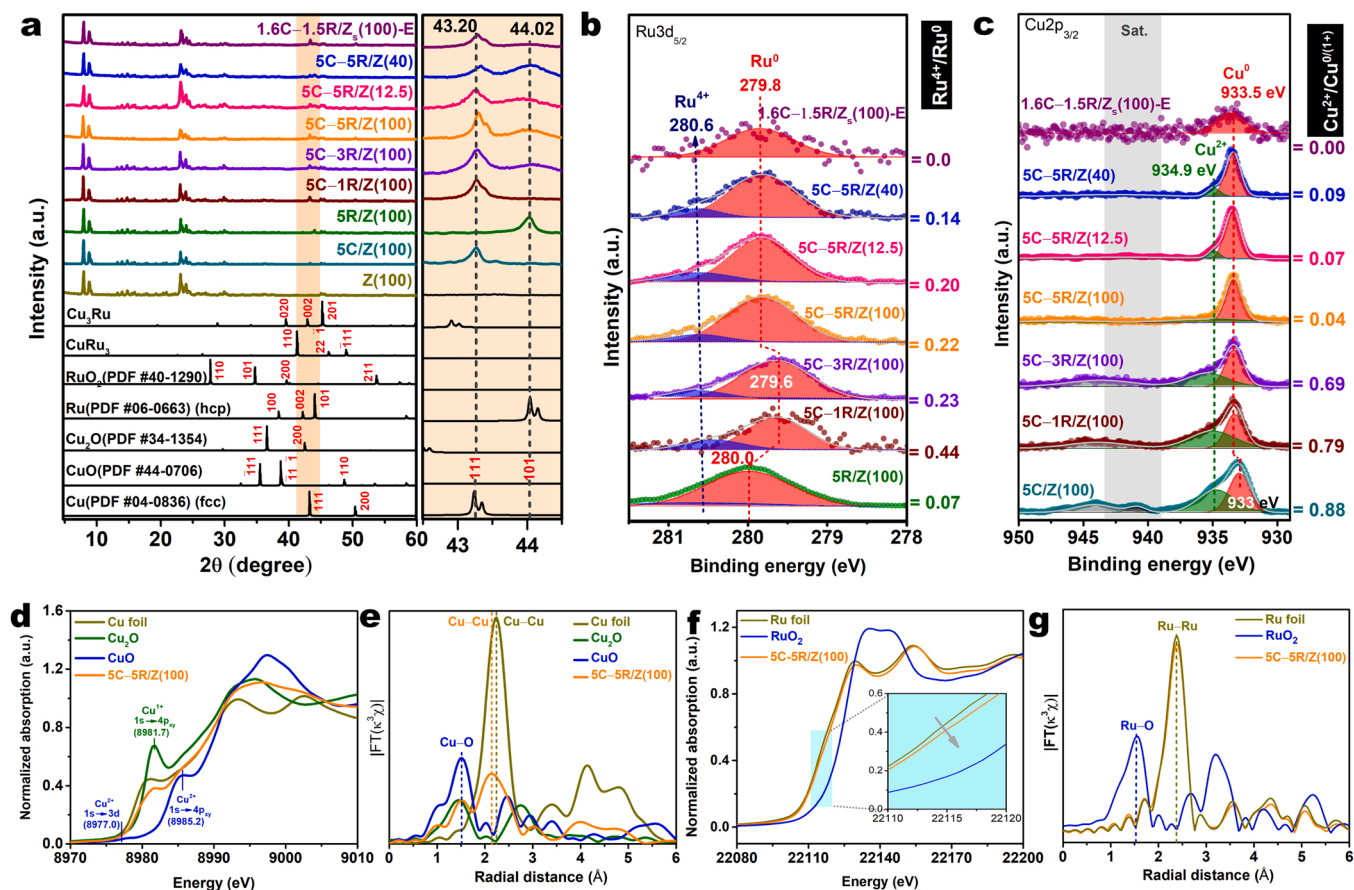
Fig. 1. (a) XRD patterns and high-resolution (b) Ru 3d$^{5/2}$ and (c) Cu 2p$^{3/2}$ XPS profiles of the mono-metallic 5Cu/Z(100) and 5Ru/Z(100) catalysts and the bi-metallic xCu–yRu/Z(100) catalysts. (d) Normalized Cu K-edge XANES spectra and (e) EXAFS profiles with k-range of 3.0–11.0 Å^{-1} of the 5 C–5 R/Z(100) catalyst, Cu foil, Cu$_2$O, and CuO standards. (f) Normalized Ru K-edge XANES spectra and (g) EXAFS profiles with k-range of 3.0–11.0 Å^{-1} of the 5 C–5 R/Z(100) catalyst, Ru foil and RuO$_2$ standards.

3. Results and discussion

3.1. Catalyst characterization

The textural properties of the zeolitic support and catalysts were evaluated using the N$_2$ adsorption–desorption isotherms, with the results shown in Fig. S3 and Table 1. The HZSM-5 supports with different Si/Al ratios exhibited type-I isotherms (International Union of Pure and Applied Chemistry (IUPAC) classification), indicating the presence of micropores. The BET surface area of the HZSM-5 support was in the range of 420–458 m^2 g^{-1} with pore volumes in the range of 2.28–2.39 cm^3 g^{-1}. As the metal loading increased, the catalysts BET surface areas and pore volumes decreased slightly, but the microporous characteristics associated with HZSM-5 were maintained.

The crystalline structures of the catalysts were examined via XRD, as shown in Fig. 1a. The intense peaks at 7–30°, which are associated with HZSM-5, were maintained after metal loading, indicating that the ARD method did not change the crystalline structure of the zeolite. The peak at $2\theta = 43.20°$ in the 5 C/Z(100) catalyst is assigned to the (111) plane of face-centered cubic (fcc) Cu^0 (PDF #04–0836), and the peak at $2\theta = 44.02°$ is assigned to the (101) plane of hexagonal close-packed (hcp) Ru^0 (PDF #06–0663). In the bi-metallic 5C–1R/Z(100) catalyst, the peak associated with Ru^0 was not observed. Conversely, the 5C–yR/Z (100) catalysts with an Ru loading of 3–5 wt% exhibited a weak and broad peak centered at $2\theta = 44.02°$. The immiscibility between the Cu and Ru phases excluded the possibility of forming a Cu–Ru alloy or intermetallic phases [36,37]. Thus, the weak and broad Ru peaks in the bi-metallic catalysts indicates that the presence of Cu NPs suppressed the growth of neighboring Ru NPs.

The chemical environment of the Ru and Cu in the catalysts were examined via XPS. The high-resolution Ru 3d$_{5/2}$ and Cu 3p$_{3/2}$ spectra were referenced to the main C 1 s peak at 284.8 eV. The Ru 3d$_{5/2}$ spectrum of the mono-metallic 5R/Z(100) catalyst can be deconvoluted into two peaks at 280.0 and 280.6 eV, which correspond to the Ru^0 and Ru^{4+} species, respectively (Fig. 1b). The Ru^0 peaks of the bi-metallic 5C–1R/Z(100) and 5C–2R/Z(100) catalysts downshifted to 279.6 eV, and those of the 5C–5R/Z(z) catalysts downshifted to 279.8 eV compared to that of 5R/Z(100). The downshifting of Ru^0 in the bi-metallic Cu–Ru catalysts indicates an electron transfer from the Cu domain to the Ru domain, which is caused by the higher electronegativity of Ru (Ru, $\chi = 2.2$; Cu, $\chi = 1.9$) [38]. The catalysts with lower Ru-to-Cu ratios exhibited a more significant downshifting effect because the transferred electrons are confined to smaller Ru domains. As the Ru content increased from 1 to 5 wt% while maintaining a Cu loading of 5 wt%, the Ru^{4+}/Ru^0 ratios decreased from 0.44 to 0.22, which confirms the electron transfer from Cu to Ru by their close proximity. The Cu 2p spectrum of the mono-metallic 5C/Z(100) catalyst shows it contains almost the same percentage of Cu^0 (at 933.0 eV) and Cu^{2+} (at 934.9 eV) species with a Cu^{2+}/Cu^0 ratio of 0.88 (Fig. 1c). As the Ru loading increased from 1 to 5 wt%, the Cu^{2+}/Cu$^{0(1+)}$ ratio decreased from 0.79 to 0.04 and the 2p → 3d shakeup satellite peak near 943.0 eV disappeared, indicating that the nearly complete reduction of Cu NPs was achieved by increasing the Ru loading. Thus, the presence of Ru NPs suppressed the re-oxidation of the Cu surface when exposed to air. The electron transfer from Cu to Ru resulted in an upshifting of the Cu^0 peak from 933.0 to 933.5 eV in the bi-metallic Ru–Cu catalysts. To
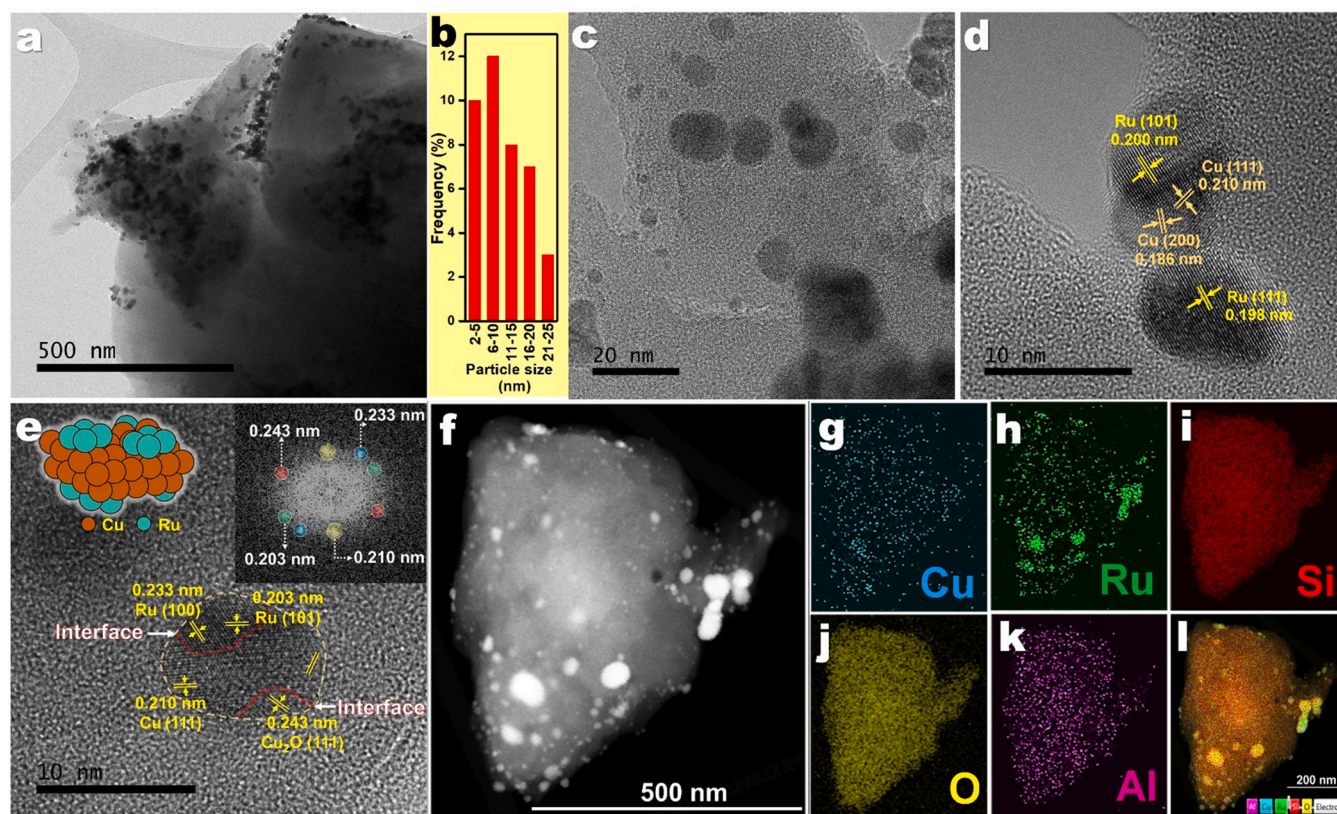
Fig. 2. (a, c, d, and e) HR–TEM images, (b) Cu and Ru NP size distributions, and (f–l) HAADF–STEM images of the 5C–5R/Z(100) catalyst and their corresponding EDS images.

differentiate Cu^0 and Cu^{1+} species, Cu LMM Auger spectrum for 5 C–5 R/Z(100) catalyst was collected (Fig. S4). The peaks at 570.1 and 568.1 eV correspond to the Cu^{1+}, and Cu^0 species [39,40], respectively, with a Cu^{1+}/Cu^0 ratio of 1.8.

To gain insight into the local structure and oxidation state of the bi-metallic 5C–5R/Z(100) catalyst, XAS analysis was performed. As shown in Fig. 1d, the Cu K-edges XANES spectrum of the 5C–5R/Z(100) catalyst did not exhibit a pre-edge peak at 8977.0 eV or a peak at 8985.2 eV, which are the characteristic $Cu^{(2+)}O$ peaks that are caused by the dipole-forbidden 1 s → 3d and dipole-allowed 1 s → $4p_{xy}$ electron transitions, respectively [41,42]. In addition, the intensity of the peak that is associated with dipole-allowed 1 s → $4p_{xy}$ electron transition of the $Cu^{(1+)}O$ species was weak in the 5C–5R/Z(100) catalyst. The adsorption edge onset upshifted compared to that of the Cu foil; this indicates that the overall valence of Cu species in the catalysts was higher than that in Cu^0, which in turn was caused by the electron transfer from the Cu domain to the Ru domain and the slight surface oxidation. The Fourier-transformed k^3-weighted EXAFS spectrum of the 5C–5R/Z(100) catalyst shows the presence of a Cu–Cu scattering path at 2.14 Å, confirming the presence of Cu^0 (Fig. 1e). The radial distance of the Cu–Cu scattering path in the Cu foil was slightly larger (2.53 Å) than that in the catalyst (2.51 Å), suggesting a higher valance state of Cu in the catalyst compared to Cu^0 (Table S3). The adsorption edge onset of the Ru K-edge XANES spectrum of the 5C–5R/Z(100) catalyst slightly upshifted as compare to the Ru foil reference, indicating that the presence of Ru oxide (Fig. 1f). The linear combination fitting of the XANES spectrum indicates approximately 4.5% RuO_2 was present in the catalyst (Table S3).

The close proximity between the Cu and Ru phases in the 5C–5R/Z(100) catalyst was examined by observing its morphology. The HR–TEM image and its image-based particle size distribution histogram show a uniform Cu and Ru NP distribution on the zeolitic support with major particle sizes in the range of 6–10 nm (Fig. 2a and b). A high-magnification HR–TEM image illustrates an asymmetric bi-metallic Cu and Ru NP shape with an interfacial boundary between the two metallic phases because of the immiscibility between the Cu and Ru phases (Fig. 2c and d) [36,37]. The lattice fringes of fcc Cu and hcp Ru NPs can be observed in the high-magnification HR–TEM image (Fig. 2e). The interlayer distances of 0.233, 0.203, 0.210, and 0.243 nm correspond to the Ru (100), Ru (101), Cu (111), and Cu_2O (111) planes, respectively. The HAADF−STEM images and their corresponding elemental mapping images show a uniform Cu and Ru NP distribution in the wide area of the support (Fig. 2f–l).

To examine the reduction behavior of the as-synthesized catalysts, H_2–TPR profiles were collected, with the results shown in Fig. 3a and Table S4. The reduction profiles were deconvoluted and divided into three low-, medium-, and high-temperature reduction zones at < 125, 125–250, and > 250 °C, respectively. The mono-metallic 5C/Z(100) catalyst exhibited two deconvoluted peaks at 197 and 236 °C, which correspond to the two-step reduction of Cu^{2+} to Cu^+ and subsequently to Cu^0, respectively [9,43]. Based on the total amounts of H_2 consumed and Cu loaded, 52.5% of the Cu was reduced to Cu^0, whereas the remaining non-reduceable Cu species (47.5%) could be present in the zeolite framework vIa ion exchange. The total amount of H_2 consumed by the reduction of the 5C/Z(100) catalyst was 0.42 mmol g^{-1}. The 5R/Z(100) catalyst exhibited two reduction peaks at 77 and 201 °C, which can be attributed to the reduction of RuO_2 to metallic Ru NPs and a strong metal–support interaction effect, respectively [44]. The total amount of H_2 consumed by the reduction of 5R/Z(100) was higher (0.78 mmol g^{-1}) than that of Cu. As the Ru content increased from 1 to 5 wt% in the bi-metallic 5C–yR/Z(100) catalysts, the reduction peak associated with $Cu^{2+} → Cu^{1+}$ downshifted; the facile reduction of Cu oxides in the presence of Ru demonstrates the close proximity between the two phases. The transfer of spillover hydrogen from the Ru domain to the Cu oxide domain could decrease the reduction temperature of Cu^{2+} [45].
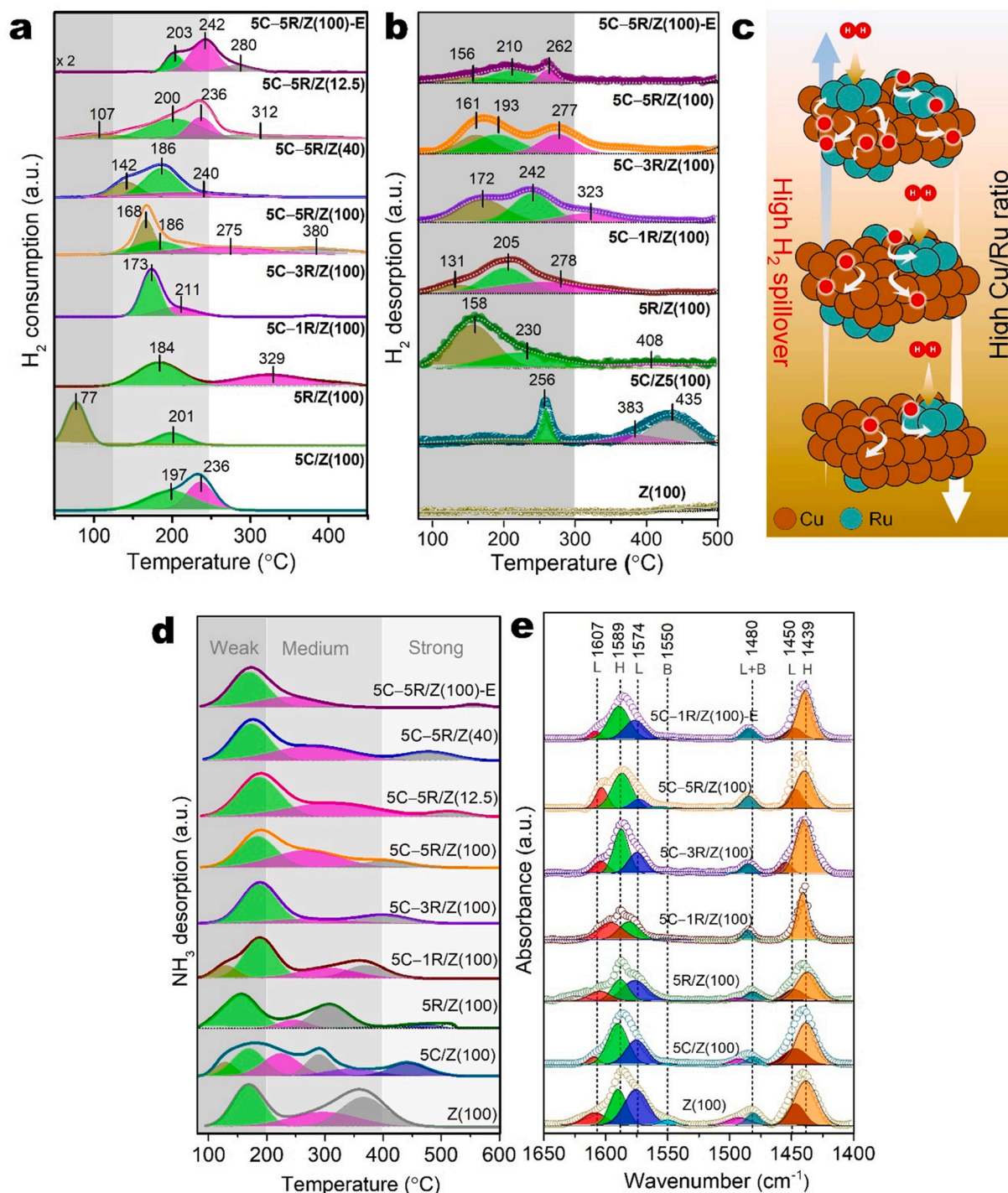
Fig. 3. (a) H$_2$–TPR profiles, (b) H$_2$–TPD profiles, (c) correlation between the Cu/Ru ratio and active H$_2$ spillover, (d) NH$_3$–TPD profiles, and (e) Py–DRIFT spectra of the mono-metallic 5Cu/Z(100) and 5Ru/Z(100) catalysts and the bi-metallic xCu–yRu/Z(100) catalysts.

The low-temperature RuO$_2$ → Ru peak at 77 °C in the mono-metallic Ru catalyst was not observed in the bi-metallic 5C–yR/Z(z) catalysts. These results imply that some Ru phase was present in the subsurface region of the Cu NPs, and thus the mild oxidation (200 °C) did not oxidize the Ru phase in the subsurface region. The total amount of H$_2$ consumed in the bi-metallic 5C–yR/Z(100) catalysts was in the range of 0.86–1.19 mmol g^{-1}, which is higher than that of the mono-metallic 5C/Z(100) and 5R/Z(100) catalysts. As the Si/Al ratio decreased to from 100 to 12.5 in the 5C–5R/Z(z) catalysts, the RuO$_2$ → Ru peak downshifted, implying that the high electron density in the Al-enriched HZSM-5 facilitated the reduction of deposited metal NPs [46,47].

The H$_2$–TPD profiles of the catalysts are shown in Fig. 3b and the amount of H$_2$ desorbed is listed in Table S5. The profiles were divided into two regions: a low-temperature region at 80–300 °C and at a high-temperature region (>300 °C). The low-temperature region corresponds to the hydrogen that is dissociated and chemisorbed on metallic sites and the hydrogen that stayed at the interface between the metal NPs and the support surface, while the high-temperature region corresponds to the hydrogen in the subsurface regions and spillover hydrogen [48,49]. Because of the lower energy barriers for the dissociated adsorption of H$_2$ on the Ru site than on the Cu site [50], the 5 R/Z(100) catalyst exhibited a prominent low-temperature hydrogen peak at 158 °C with a much

Table 2
Acidic, H$_2$ desorption, and H$_2$ reduction properties of the zeolite supports, mono-metallic Ru and Cu catalysts, and bi-metallic xCu–yRu/Z(z) catalysts.

Catalyst	Acidity[a] (mmol g^{-1})				L/B[b] ratio	H$_2$ desorption[c] (mmol g^{-1})	H$_2$ adsorption[d] (mmol g^{-1})
	Weak (<250 °C)	Medium (250–400 °C)	Strong (>400 °C)	Total			
Z(100)	0.05	0.11	0.01	0.17	9.5	0.005	N.A.
Z(40)	0.18	0.37	0.28	0.83	N.A.	N.A.	N.A.
Z(12.5)	0.22	0.53	0.41	1.16	N.A.	N.A.	N.A.
Z$_s$(100)	0.06	0.11	0.02	0.18	N.A.	N.A.	N.A.
5C/Z(100)	0.06	0.07	0.02	0.15	16.0	0.06	0.42
5R/Z(100)	0.06	0.07	0.01	0.14	13.4	0.19	0.78
5C–1R/Z(100)	0.05	0.07	0.01	0.13	20.0	0.14	0.86
5C–3R/Z(100)	0.06	0.04	0.01	0.11	23.2	0.15	0.96
5C–5R/Z(100)	0.04	0.05	0.01	0.10	24.0	0.19	1.28
5C–5R/Z(40)	0.21	0.28	0.16	0.65	N.A.	N.A.	1.25
5C–5R/Z(12.5)	0.28	0.32	0.19	0.79	N.A.	N.A.	1.39
5C–5R/Z(100)-S[e]	0.05	0.05	0.01	0.11	N.A.	N.A.	0.66
5C–5R/Z(100)-E	0.06	0.06	0.01	0.13	25.6	0.10	0.30
5C–5R/Z1(100)@ SiO$_2$	N.A.	N.A.	N.A.	N.A.	N.A.	0.17	1.06
5C–5R/Z1(100)@ C	N.A.	N.A.	N.A.	N.A.	N.A.	0.18	1.39

[a] Measured via NH$_3$–TPD.
[b] L/B = Lewis/Brønsted acid site ratio that was determined from Py–DRIFT.
[c] Hydrogen desorption that was calculated via H$_2$–TPD.
[d] Hydrogen consumption that was calculated via H$_2$–TPR.
[e] After the 1st run, the spent catalyst was washed with water and acetone followed by drying at 80 °C. Then, the dried catalyst was calcined at 550 °C in air followed by activation at 450 °C for 4 h in a H$_2$/Ar flow.

higher amount of H$_2$ desorption (0.195 mmol g^{-1}) compared to those of Cu (256 and 435 °C; 0.058 mmol g^{-1}). In the bi-metallic catalysts, the high-temperature desorption peak of 5C/Z(100) at 435 °C disappeared and most of the hydrogen was desorbed in the low-temperature region. In addition, as the Ru loading in the 5C–yR/Z(100) catalysts increased, the amount of hydrogen desorbed increased from 0.145 to 0.190 mmol g^{-1}. Based on the H$_2$–TPD and H$_2$–TPR data, it can be concluded that the contact between the Ru and Cu domains lead to the facile transport of the dissociated hydrogen on the Ru sites to the Cu sites (Fig. 3c).

To examine the total acidity of the catalysts, NH$_3$–TPD profiles were collected, with the results shown in Fig. 3d and Table 2. The NH$_3$–TPD profiles were categorized into three regions: weak (<250 °C), medium (250–400 °C), and strong (>400 °C). The weak acid sites corresponded to the NH$_3$ interactions with the cation-bonded and terminal silanol groups, the medium acid sites were assigned to the NH$_3$ interaction with acidic protons at the bridging Si–(OH)–Al sites, and the strong acid sites corresponded to the NH$_3$ interactions with the extra Al framework of the Si–(O)–Al site [51,52]. The mono- and bi-metallic catalysts exhibited a decrease in the medium acidity compared to the Z(100) support, which implies the preferential ion exchange and deposition of metal NPs on the bridging Si–(OH)–Al sites. The evolution of the high-temperature desorption peak centered at 445 °C in the 5C/Z(100) catalyst indicates that the metallic Cu NPs generated strong Lewis acid centers [53]. The bi-metallic 5C–yR/Z(100) catalysts did not exhibit a strong desorption peak, which could be caused by the close proximity between the Ru and Cu domains. As the Ru loading in the bi-metallic 5C–yR/Z(100) increased from 1 to 5 wt%, the total acidity decreased from 0.15 to 0.10 mmol g^{-1}. The appearance of strong acid peaks in the 5C–5R/Z(12.5) and 5C–5R/Z(40) catalysts confirm the existence of extra aluminum frameworks.

To further investigate the nature of acid sites, py–DRIFT spectra were collected, as shown in Fig. 3e. The adsorption bands associated with the 8a, 8b, and 19b pyridine ring vibration (ν_{CCN}) were observed in the frequency range of 1650–1400 cm^{-1} [54]. Pyridine coordinates to LASs (L-Py or L) or protonated on BASs (HPy$^+$ or B), which appears as a band pair near 1450/1607 and 1550/1635 cm^{-1}, respectively [54,55]. In addition, the bands that appeared at 1589 cm^{-1} originated from the weak interaction between pyridine and low electron-withdrawing LASs [56]. The areas under the infrared band at 1550 and 1450 cm^{-1} were selected to calculate the L/B ratios; these results are summarized in Table 2. Because of the preferential metal NP deposition on the bridging

Si–(OH)–Al sites and ion exchange, the L/B ratios of the mono- and bi-metallic catalysts were much larger (13.4–25.6) than that of the pristine zeolitic support (9.5).

3.2. Catalytic biomass conversion

The chemical species produced from the conversion of raw ligno-cellulose biomass over the mono- and bi-metallic catalysts can be categorized into LDPMs (such as (propyl-substituted) guaiacols (G) and (propyl-substituted) syringols (S)), cellulose- and hemicellulose-derived monomers (such as ketones (KNs), which include cyclic (CKs) and linear (LKs) ketones), reaction intermediates (such as glucose (GLU), 5-HMF, and levulinic acid (LVA)), and byproducts (such as alcohols/alkanes (ALC) and acetic acid (AA)). As shown in Fig. 4a, in the absence of a catalyst, oakwood conversion was 82% at 300 °C under an initial H$_2$ pressure of 3.0 MPa for 1 h. The yields of the LDPMs and KNs that were collected in the DSPs were low (1.5% and 1.3%, respectively), while acid-hydrolyzed species from holocellulose, such as GLU (18.0%), 5-HMF (5.6%), AA (2.1%), and LVA (1.2%), were found in greater amounts in the WSPs. The LDPMs include guaiacol, 4-ethyl guaiacol, and syringaldehyde, and the KNs include 2-CPeO, 2-mCPeO, and 3-hydroxybutan-2-enone (Fig. S5). The total yield of quantified products obtained from the oakwood conversion in the absence of catalyst was approximately 35%; the other non-quantifiable products (approximately 47%) can correspond to dimers, oligomers, and high-molecular-weight species that were not detected by GC/TOF–MS and GC–FID and that could not be quantified by HPLC. Over the Z(100) support, the oakwood conversion increased to 95% with the yields of LDPMs and KNs of 2.0% and 3.8%, respectively. The total yield of WSPs slightly decreased to 23.5% as compare to the blank case (27.4%). Over the 5C/Z (100) catalyst, the oakwood conversion increased to 96%, and the targeted LDPM and KN yields increased to 7.6% and 8.2%, respectively. When the 5R/Z(100) catalyst was tested, the LDPM and KN yields further increased to 27.9% and 27.0%, respectively. Thus, active hydrogen availability plays an important role in the synthesis of desirable monomers. The LDPM and KN yields over the bi-metallic 5C–1R/Z (100) and 5C–3R/Z(100) catalysts were similar to those of the 5R/Z (100) catalyst. Over the bi-metallic 5C–5R/Z(100) catalyst, the oakwood was almost completely converted, and the LDPM and KN yields increased significantly to 28.4% and 60.9%, respectively. The major LDPMs include propyl-substituted guaiacol and syringol with yields of 10.3% G and 18.3% S, respectively. The major CKs include CPO, mCPO,
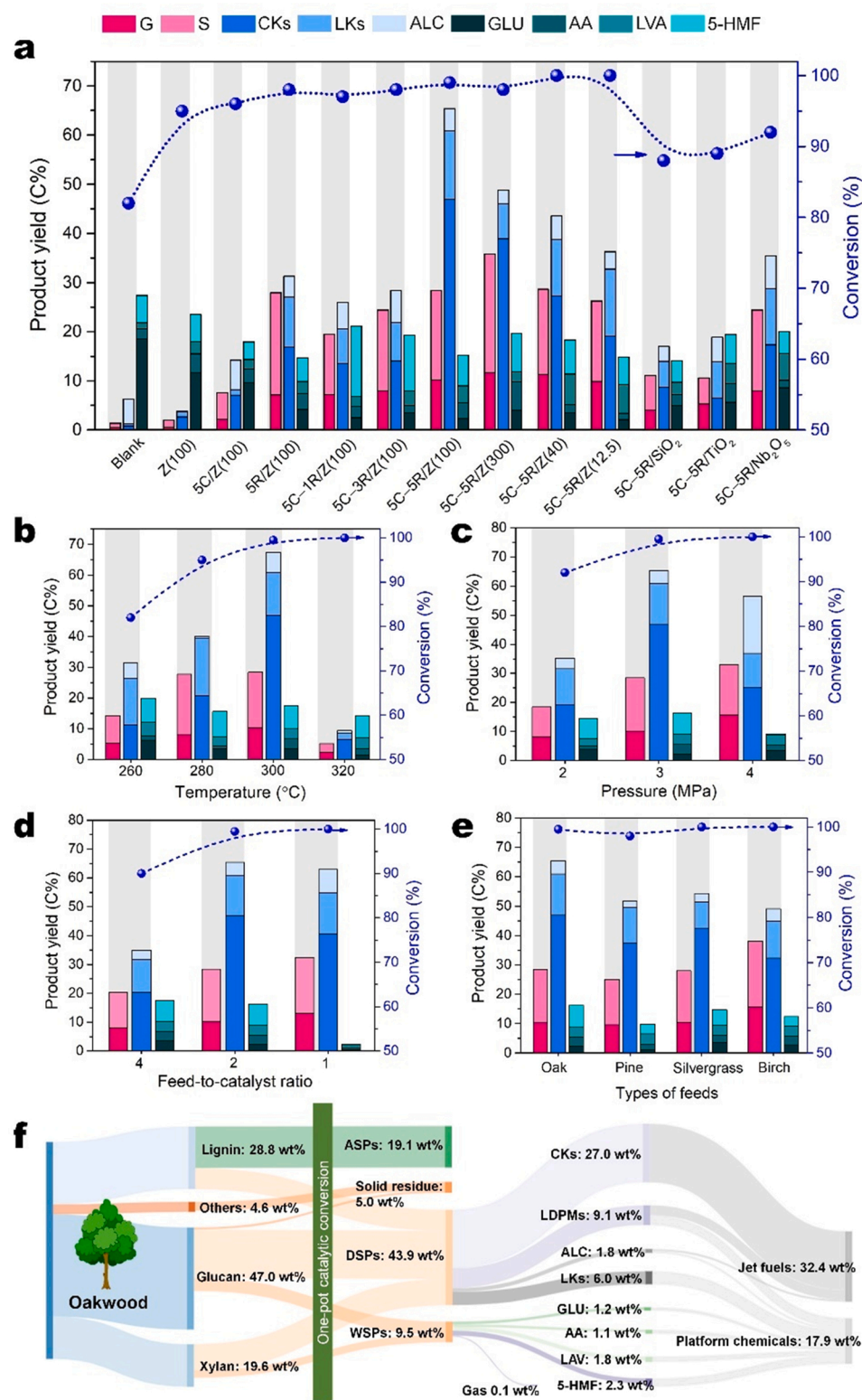
Fig. 4. (a) Oakwood conversion and product yield over various types of catalysts. Reaction conditions: 0.5 g of oakwood, 30 mL of H_2O, a feed-to-catalyst ratio of 2, a temperature of 300 °C, an initial H_2 pressure of 3.0 MPa, and a duration of 1 h. Effect of (b) reaction temperature, (c) initial H_2 pressure, (d) feed-to-catalyst ratio, and (e) feedstock type on biomass conversion and product yield, and (f) Sankey diagram of complete oakwood biomass conversion based of the weight of glucans + xylans + lignin. Reaction conditions (Δ reaction temperature): 0.5 g of oakwood, 30 mL of H_2O, a feed-to-catalyst ratio of 2, an initial H_2 pressure of 3.0 MPa, and a duration of 1 h. (Δ H_2 pressure): 0.5 g of oakwood, 30 mL of H_2O, a feed-to-catalyst ratio of 2, a temperature of 300 °C, and a duration of 1 h. (Δ catalyst-to-feed ratio): 0.5 g of oakwood, 30 mL of H_2O, a temperature of 300 °C, an initial H_2 pressure of 3.0 MPa, and a duration of 1 h. (Δ feedstock): 0.5 g of feedstock, 30 mL of H_2O, a feed-to-catalyst ratio of 2, a temperature of 300 °C, an initial H_2 pressure of 3.0 MPa, and a duration of 1 h. Gray bar: OSPs; white bar: WSPs.

and 2-mCPeO with a yield of 46.9% and the major LKs include 2,5-hexanedione, 2-pentanone, and 5-hydroxy-2-heptanone with a yield of 14.0% (see the GC–TOF/MS chromatogram of the DSP in Fig. S6 and a list of chemical species in Table S6). In the WSPs, other valuable chemicals such as GLU (2.3%), 5-HMF (6.2%), AA (3.2%), and LVA (3.5%) were present. To examine the possibility of the presence of high-molecular-weight species in the WSPs, a GFC analysis was performed

(Fig. S7). The two sharp peaks at the elution volumes of 21–23 min indicates the presence of high-molecular-weight species, which could be humins, lignin-derived oligomers, and unconverted holocellulose-derived intermediates. Negligible amounts of gaseous products (<1%) that include C_1–C_6 were detected during the oakwood conversion (Fig. S8). As the Si/Al ratio of HZSM-5 increased to 300 in the 5C–5R/Z (300) catalyst, KNs yield decreased to 46.1% with an increase in the

Table 3
Various types of biomass conversion over the 5C–5R/Z(100) catalyst.[a]

Feedstock	DSP[b] yield (%)				WSP[c] yield (%)					Carbon balance (%)
	CKs	LKs	ALC	Total	GLU	5-HMF	AA	LVA	Total	
Cellulose	8.9	32.1	14.7	55.7	8.9	3.2	N.D.[d]	6.2	18.3	76.0
Glucose	13.5	34.4	12.5	60.4	N.D.	4.7	N.D.	7.7	12.4	72.8
Fructose	11.8	38.5	< 2	51.3	N.D.	5.0	N.D.	5.2	10.2	61.5
Xylose	10.8	21.5	15.6	47.9	N.D.	N.D.	N.D.	8.9	8.9	56.8

[a] Reaction conditions: 0.5 g of feedstock, 30 mL of water, a temperature of 300 °C, an initial H_2 pressure of 3.0 MPa, a feed-to-catalyst ratio of 2, and a duration of 1 h.
[b] CKs: cyclic ketones; LKs: linear ketones; ALC: alcohols and alkanes
[c] GLU: glucose; 5-HMF: 5-hydroxymethylfurfural; AA: acetic acid; LVU: levulinic acid
[d] N.D.: Not detected

LDPM yield to 35.8%. As the Si/Al ratio of H-ZSM5 decreased to 40 and 12.5 in the 5C–5R/Z(*z*) catalysts, the KN yields decreased to 33.8% and 32.8%, respectively, while the LDPM yields were maintained. The decreased KN yield at low Si/Al ratios indicates that the presence of highly acidic sites (Table 2) could promote humin formation via reactive intermediates polymerization (e.g., 5-HMF and FFA) in the aqueous medium [57]. To further examine effect of acidic sites, bi-metallic Cu–Ru supported on SiO_2 (total acidity of 0.001 mmol g^{-1}), TiO_2 (total acidity of 0.031 mmol g^{-1}), and Nb_2O_5 (total acidity of 0.055 mmol g^{-1}) catalysts were synthesized and tested. The KN yields are in the following order: 5C–5R/Nb_2O_5 (18.7%) > 5C–5R/TiO_2 (13.9%) ≈ 5C–5R/SiO_2 (14.0%); the LDPM yields are in the following order: 5C–5R/Nb_2O_5 (24.5%) > 5C–5R/TiO_2 (10.7%) ≈ 5C–5R/SiO_2 (11.1%) at an oakwood conversion of approximately 90%. It is noted that highest KN yield was achieved over the 5C–5R/Z(100) catalyst with a total acidity of 0.10 mmol g^{-1}. The use of 5C–5R/Nb_2O_5 with a total acidity of 0.055 mmol g^{-1} that was lower than 5C–5R/Z(100) or 5C–5R/Z(12.5) with a total acidity of 0.79 mmol g^{-1} that is higher than 5C–5R/Z(100) resulted in lower KN yields than that of 5C–5R/Z(100). Under the highly acidic condition, the formation of undesirable humins is activated, while under the low acidic condition, the cleavage of glycosidic linkage, isomerization, and dehydration to produce 5-HMF and FFA are suppressed. Thus, the acidic sites play an important role in the complete biomass conversion.

To optimize the reaction conditions, parameters such as temperature, pressure, and feed-to-catalyst ratio were varied. As the temperature increased from 260° to 300°C, both the oakwood conversion and LDPM and KN yields increased (Fig. 4b). A further increase in temperature to 320 °C resulted in a decrease in the LDPM and KN yields, which could be due to reaction intermediates repolymerization or product decomposition. The initial amount of H_2 plays a significant role in product yield, as shown in Fig. 4c. As the initial H_2 pressure decreased from 3.0 to 2.0 MPa, a significant decrease in the LDPM and KN yields was observed. As the H_2 pressure increased from 3.0 to 4.0 MPa, the LDPM yield slightly increased, while the KN yield decreased. Thus, a high H_2 pressure promotes the cleavage of β–O–4 linkage in the native lignin [15]. The decreased KN yield and increased ALC yield with increasing H_2 pressure suggests the over hydrogenation of the reaction intermediates (e.g., 2,5-DMF and 2,5-HDN). At feed-to-catalyst ratios ≥ 2, the oakwood conversion and LDPM and KN the yields were maintained (Fig. 4d). The reaction in lower alcohols (e.g., methanol and ethanol) did not selectively convert oakwood to LDPMs and KNs (Fig. S9), indicating that aqueous medium plays a role in controlling the reaction pathways.

At optimum conditions (temperature = 300 °C, initial H_2 pressure = 3 MPa of H_2, and feed-to-catalyst ratio = 2 for 1 h), different types of raw biomass materials were tested over the 5C–5R/Z(100) catalyst (Fig. 4e). The yield of KNs synthesized from pinewood, silvergrass, and birchwood were in the range of 49–54%, and that of LDPMs were in the range of 25–38%. The LDPMs produced from birchwood exhibited a higher yield because of their higher S/G ratios compared to the other woods; the richer β–O–4 bond in the lignin structure facilitates monomer production by the cleavage of the low-energy bond [15]. As shown in

Fig. 4f, based on the total weight of oakwood, 27 wt% CKs, 9.1 wt% LDPMs, and 1.8 wt% ALC could be produced, which could be used as feedstock for jet fuel production. In addition, platform chemicals such as LKs, GLU, LVA, and 5-HMF with a total yield of 17.3 wt% could be produced by the oakwood conversion.

3.3. Reaction pathway

The reaction mechanisms for the conversion of intact lignin in raw biomass to LDPMs have been discussed in previous studies (e.g., β–O–4 linkage hydrolysis/solvolysis and subsequent reacted monomer intermediates stabilization) [58], however, the direct consecutive conversion of holocellulose to KNs has not been discussed to date. Herein, to understand the holocellulose conversion mechanisms over the 5C–5R/Z (100) catalyst, model saccharides, such as cellulose, glucose, fructose, and xylose, were converted over the catalyst, and the results are listed in Table 3. The yields of LKs synthesized from the model saccharides are larger than those of CKs. This reaction behavior is different from that observed in the raw biomass conversion; the yields of LKs from the raw biomass were lower than those of CKs (Fig. 4e). To explain the difference in the LK and CK yields, we hypothesize that lignin-derived oligomers or monomers could interfere with the holocellulose-derived intermediates adsorption. To examine our hypothesis, cellulose was reacted over the 5C–5R/Z(100) catalyst in the presence of phenol as a model lignin monomer. The product distribution in the presence of phenol (Fig. S10b) was similar to that without phenol (Fig. S10a), which indicates that the presence of LDPMs did not play a significant role in changing the reaction pathways. When the cellulose conversion was conducted in the presence of lignin-derived oligomers collected after the oakwood reaction, the major cellulose-derived products were CKs (Fig. S11). Therefore, pre-adsorbed lignin-derived oligomers on the active sites prohibited the subsequent adsorption of holocellulose-derived intermediates because of their high adsorption energy [59], which can retard the reaction to CKs (Fig. 5a).

Based on the analysis of the products from the oakwood conversion and the model polysaccharides, plausible reaction pathways are shown in Fig. 5b. Under hydrothermal conditions, the glycosidic, ether, and ester linkage present in the raw biomass are cleaved via hydrolysis promoted by acidic-rich protons in subcritical water and by the BASs of ZSM-5, resulting in monosaccharide production (e.g., glucose and xylose). Then, some glucose fraction is isomerized to fructose over the LASs. Fructose and xylose dehydration over the acid sites produces their corresponding furanic aldehydes, namely, 5-HMF and FFA, respectively. The 5-HMF and FFA could separately follow different reaction routes to form 3-mCPO and CPO, respectively. A plausible route for the 5-HMF-to-3-mCPO conversion involves the following: (1) hydrodeoxygenation of 5-HMF to 2,5-DMF over the metallic site; (2) hydration and subsequent ring opening of 2,5-DMF to 2,5-hexadione (2,5-HDN) over the acidic site; (3) intramolecular aldol condensation of 2,5-HDN to 3-methylcy-clopenten-2-one (3-mCPeO) over the acidic stie; and (4) hydrogenation of 3-mCPeO to 3-mCPO over the metallic site [60,61]. In the FFA-to-CPO case, a plausible route involves the following steps: (i)
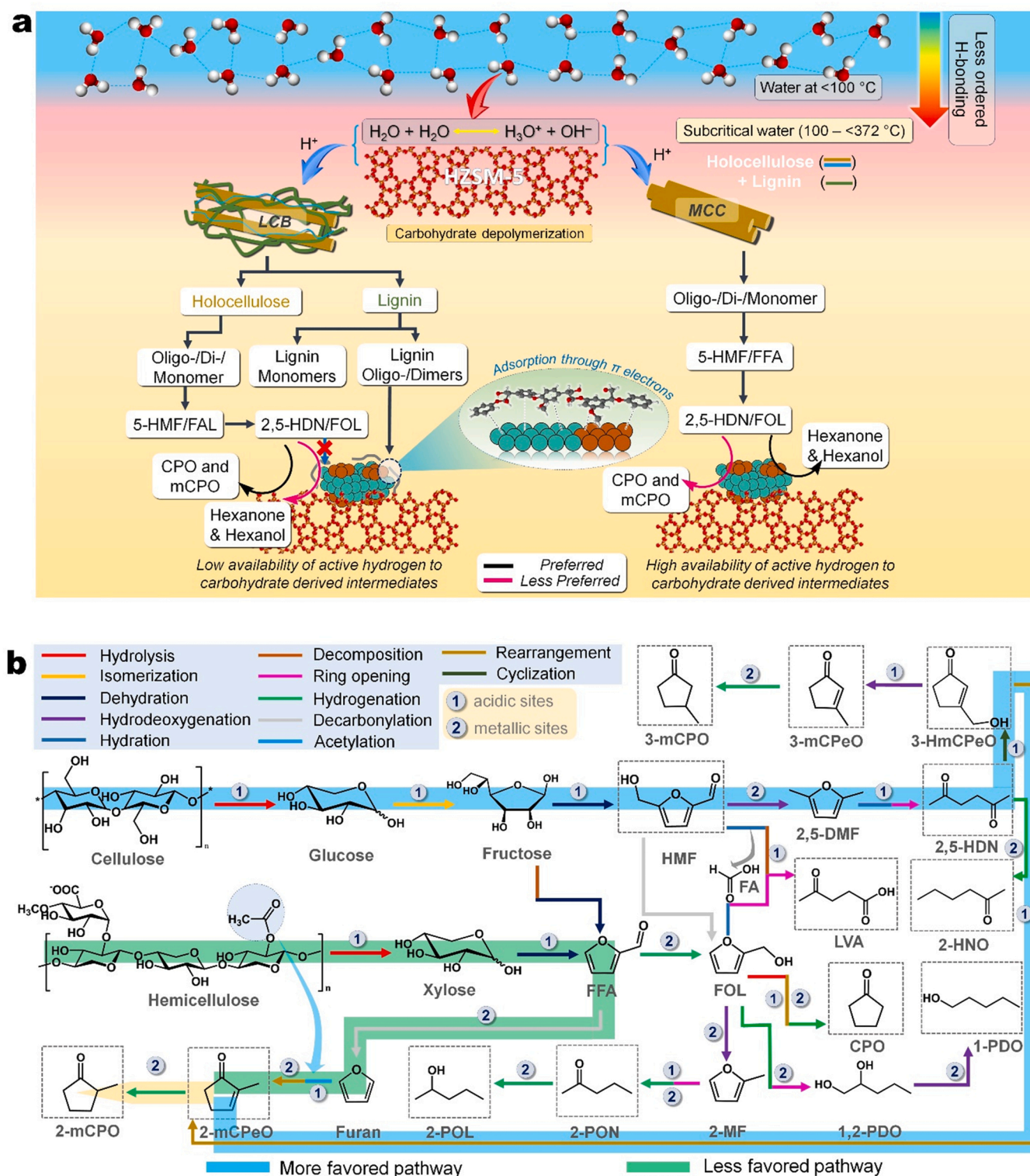
Fig. 5. (a) Schematic of lignocellulosic biomass depolymerization over the 5C-5R/Z(100) catalyst under subcritical water conditions and the role of in situ-produced oligomeric lignin in cyclic ketone production. (b) Plausible reaction pathway for cyclic and linear ketones formation.

hydrogenation of FFA to FOL over the metallic site; (ii) carbocation species formation over BASs and subsequent ring opening, which proceeds to cyclic rearrangement to produce 3-hydroxycyclopentanone; (iii) dehydration of 3-hydroxycyclopentanone to cyclopent-2-enone (2-CPeO); and (iv) hydrogenation of 2-CPeO to CPO [24–27,62,63]. However, the 5-HMF-to-3-mCPO and FFA-to-CPO pathways could not capture the production of 2-mCPeO and 2-mCPO observed in the raw

biomass conversion (Fig. S6).

To propose plausible reaction pathways from the lignocellulosic biomass conversion to 2-mCPeO and 2-mCPO, several model reactions were investigated. First, 2,5-DMF conversion over the 5C–5R/Z(100) catalyst resulted in two major 2-hexanone (2-HNO) and 3-mCPO species along with 1-methylcyclopn-2-enol (1-mCPeL) as a minor product (Fig. S12); this indicates that 2,5-DMF is not an intermediate for 2-
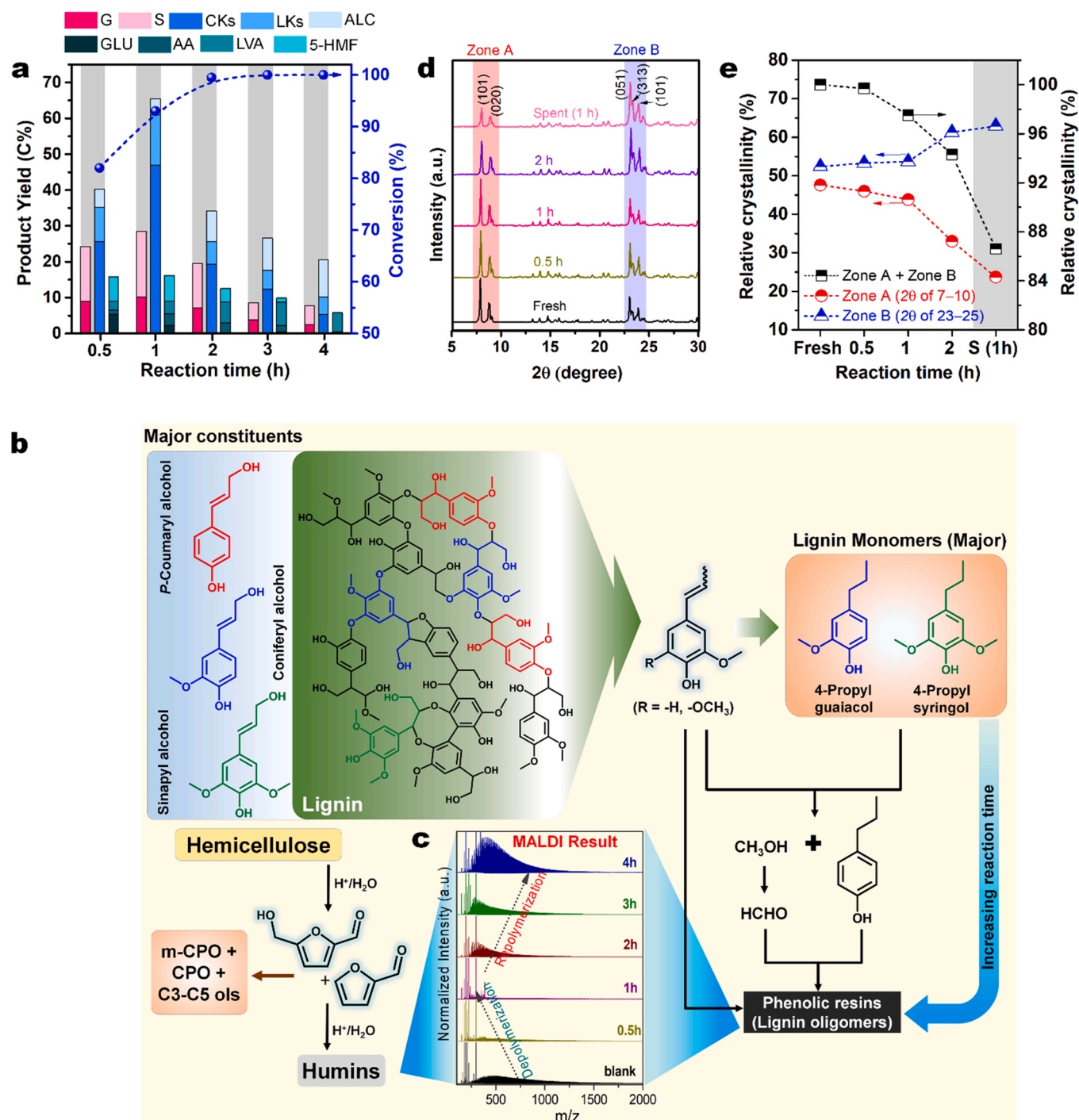
Fig. 6. (a) Effect of time on oakwood conversion and product yield over the 5C–5R/Z(100) catalyst. Gray bar: OSPs; white bar: WSPs. (b) Schematic of oligomer or humin formation in the extended reaction time period. (c) MALDI–TOF/MS profiles of the DSPs that were collected at varying reaction times. (d) XRD patterns of the spent 5C–5R/Z(100) catalysts that were collected at varying reaction times. (e) Effect of reaction time on the crystallinity of the spent 5C–5R/Z(100) catalysts. Reaction conditions: 0.5 g of oakwood, 30 mL of H_2O, a feed-to-catalyst ratio of 2, a temperature of 300 °C, an initial H_2 pressure of 3.0 MPa, and a duration of 1 h. The relative crystallinity percentage ($2\theta = 5$–$35°$) was calculated as follows: $RC\% = I_c/I_c + I_a$, where I_c and I_a are the total crystallinity of the crystalline and amorphous peaks, respectively.

mCPeO and 2-mCPO formation. Hydrodeoxygenation of 2,5-HDN could not produce 2-HNO. To understand the pathway for 1-mCPeL formation from 2,5-DMF, 3-mCPeO, which is an intermediate produced from 2,5-DMF (Fig. 5b), was reacted over the 5C–5R/Z(100) catalyst (Fig. S13). The major product was 3-mCPO, but the presence of a small amount of 1-mCPOL indicates that 1,3-methyl shift in 3-mCPeO occurred, which produced 1-mCPeL as an intermediate for 1-mCPOL production. To examine another possibility, 5-HMF was reacted over the 5C–5R/Z(100)

catalyst (Fig. S14). In this reaction, 2-mCPO was one of the major products along with 3-mCPeO. Therefore, 5-HMF is the key intermediate to produce 2-mCPO. As shown in Fig. S15a, the 5-HMF-to-2,5-DMF conversion could follow two pathways: (1) hydrogenolysis of the hydroxyl group in 5-HMF produces 5-methylfurfural (5-MFA), hydrogenation of the carbonyl group in 5-MFA produces 5-methylfuranmethanol (5-MFM), and subsequent hydrogenolysis of 5-MFM produces 2,5-DMF; and (2) hydrogenation of carbonyl group in 5-HMF
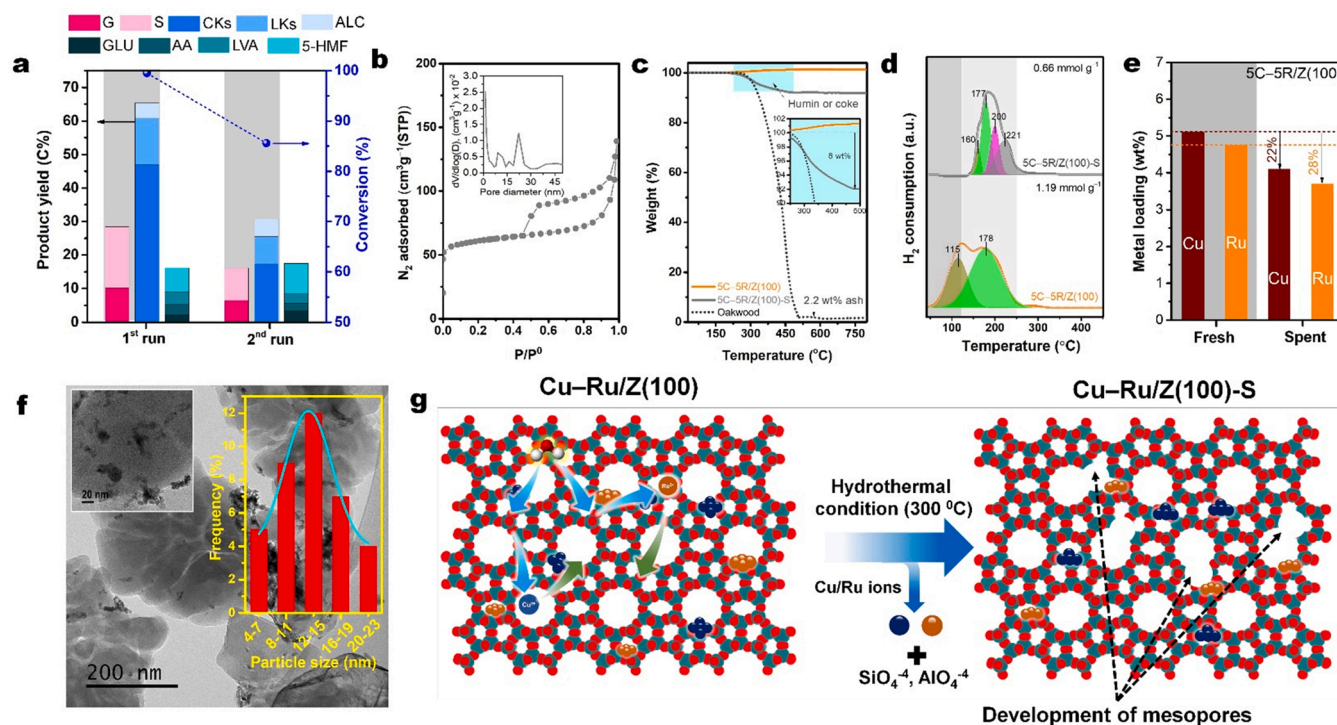
Fig. 7. (a) Catalyst reusability test results. (b) N_2 adsorption–desorption isotherm of the spent 5C–5R/Z(100)-S catalyst (inset: BJH profile). (c) TGA profiles, (d) H_2–TPR profiles, and (e) ICP–OES data of the fresh 5C–5R/Z(100) and spent 5C–5R/Z(100)-S catalysts. (f) TEM image of the 5C–5R/Z(100)-S catalyst (Inset: a magnified TEM image and histogram of metal NPs). (g) Schematic for the formation of mesopores in the spent 5C–5R/Z(100)-S catalyst. Reaction conditions: 0.5 g of oakwood, 30 mL of H_2O, a feed-to-catalyst ratio of 2, a temperature of 300 °C, an initial H_2 pressure of 3.0 MPa, and a duration of 1 h.

produce 2,5-bis(hydroxymethyl)-furan (2,5-BHMF), hydrogenolysis of hydroxyl group in 2,5-BHMF produces 5-MFM, and subsequent hydrogenolysis of the remaining hydroxyl group in 5-MFM produces 2,5-DMF [3]. Ring opening of 5-MFM via hydration followed by hydrogenation could produce 1-hydroxyhexane-2,5-dione (HHDN), and subsequent intramolecular aldol condensation of HHDN could produce 3-(hydroxymethyl)-cyclopent-2-enone (3-HmCPeO). Through dehydration, the acidic sites could initiate an intermediate carbocation transition stage from 3-HmCPeO (**Pathway I,** Fig. S15a). This intermediate carbocation could follow two different routes to produce 2-mCPO and cyclohexanone (CHN) via hydride shift. Thus, HHDN could be used as an intermediate to produce 2-mCPeO and 2-mCPO.

The presence of CPO in the cellulose (Fig. S10), fructose (Fig. S16), and 5-HMF (Fig. S14) conversion indicates the feasibility of decarbonylation of 5-HMF to FOL [64] over the 5C–5R/Z(100) catalyst (Fig. 5b). Similarly, 2-acetylfuran (2-AF) formation from the fructose conversion (Fig. S16; compound no. 11) confirms that decarbonylation of FFA to furan [64,65] and the subsequent acetylation of furan to 2-AF occurred. The decarbonylation of FFA to furan was previously observed over the Ru [65] and Cu [66] catalysts. In addition, the acylation of furan ring can be favored because of the high stability of AA acyl species in the HZSM-5 micropores [67]. AA tends to form from cellulose decomposition under hydrothermal conditions [68]. When 2-AF was reacted over the 5C–5R/Z(100) catalyst, 2-mCPeO and 2-mCPO formation along with 3-hexanone (3-HNO) and CHN as minor products were observed (Fig. S17). Based on the above observation, a new reaction pathway based on 2-AF is proposed (**Pathway II,** Fig. S15b). In the proposed pathway, 2-AF could follow three different reaction pathways: (1) hydrogenation of ketonic group in 2-AF followed by ring opening and recyclization to produce 3-hydroxy-2-methylcyclopentanone (3-HmCPO), and subsequent dehydration and hydrogenation of 2-HmCPO to 2-mCPO; (2) ring opening of 2-AF followed by

hydrogenation to produce 5-oxohexanal, and cyclization of 5-oxohexanal via intramolecular aldol condensation to produce cyclohex-2-enone (2-CHeN) followed by hydrogenation of 2-CHeN to produce cyclohexanone (CHN); and (3) hydrodeoxygenation of ketonic group in 2-AF to produce 2-ethylfuran (2-EF), ring opening of 2-EF to produce hex-4-en-3-one (4-HeNO), and subsequent hydrogenation of 4-HeNO to 3-hexanone (3-HNO).

3.4. DRIFT spectra of FFA adsorption on mono-/bi-metallic Cu–Ru catalysts

The adsorption geometry of reaction intermediates on the catalyst surface is one of factors that determine the product selectivity. Over the 5C–5R/Z(100) catalyst, CKs were predominant in the reaction products (Fig. 4a and Table S6). FFA is one of the key intermediates for the formation of CPO and 2-mCPO (Fig. 5b and Fig. S15b). Therefore, in this section, the adsorption behaviors of FFA on the mono-/bi-metallic Cu–Ru catalysts were investigated, as shown in the FFA–DRIFTS profiles (Fig. S18). Gas-phase FFA shows four characteristic bands at 1720, 1570, 1474 and 1395 cm^{-1}, which correspond to $\nu(C=O)$, ring breathing, $\nu(C=C)$, and $\nu(C–C) + \nu(CH)_{CHO}$, respectively [44,69]. The $\nu(C=O)$ band was red-shifted to 1685 cm^{-1} over the mono-metallic 5C/Z(100) and 5R/Z(100) catalysts and the bi-metallic 5C–1R/Z(100) and 5C–3R/Z(100) catalysts. A more significant red shift of the $\nu(C=O)$ band to 1673 cm^{-1} was observed over the 5C–5R/Z(100) catalyst. The increase in the Ru loading did not decrease the intensity of the bands that are associated with ring breathing and $\nu(C=C)$, indicating the η^1-(O)-aldehyde configuration was maintained; this is because of the overlapping between the fully occupied 3d band of the Cu metal the antibonding orbital of the furan ring [70,71]. The strong interaction between C=O bond of FFA and the catalyst surface could favor the formation of FOL [44,69] or furan intermediate, which leads to form
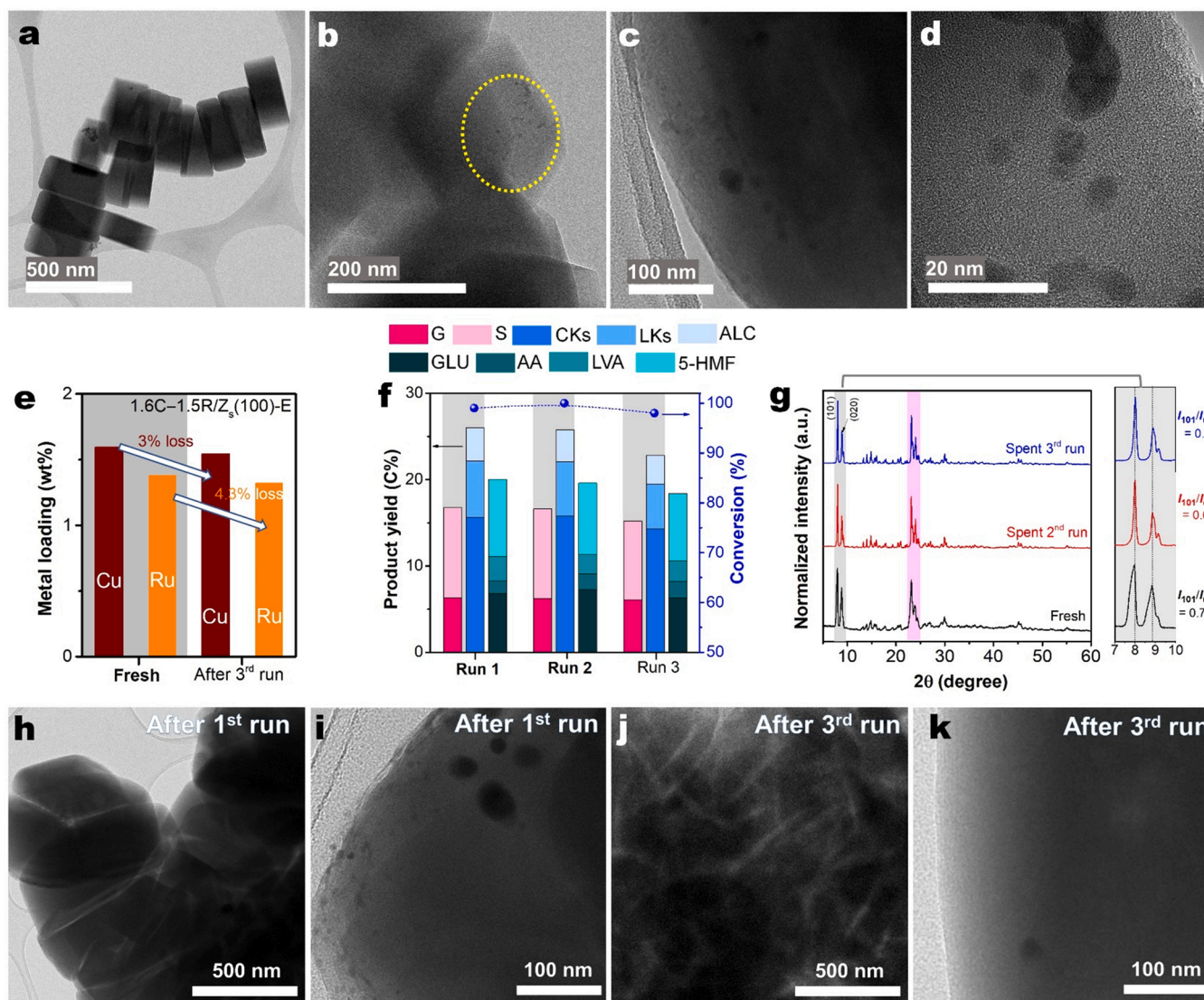
Fig. 8. (a–d) HR–TEM images of the fresh 1.6C–1.5R/Z$_s$(100)-E catalyst. (e) ICP–OES data of the fresh and spent 1.6C–1.5R/Z$_s$(100)-E catalysts. (e) Reusability results of the 1.6C–1.5R/Z$_s$(100)-E catalyst. (g) XRD patterns of the fresh and spent 1.6C–1.5R/Z$_s$(100)-E catalysts. HR–TEM images of the spent 1.6C–1.5R/Z$_s$(100)-E catalysts that were collected after the (h and i) 1st and (j and k) 3rd runs. The relative crystallinity percentage ($2\theta = 5$–35°) was calculated as follows: RC% = I_c/ I_c+I_a, where I_c and I_a are the total crystallinity of the crystalline and amorphous peaks, respectively. Reaction conditions: 0.5 g of oakwood, 30 mL of H$_2$O, a feed-to-catalyst ratio of 2, a temperature of 300 °C, an initial H$_2$ pressure of 3.0 MPa, and a duration of 1 h.

CPO and 2-mCPO (Fig. 5b).

3.5. Catalyst deactivation

To examine the stability of the bi-metallic xC–yR/Z(100) catalyst under hydrothermal conditions, time course reactions were performed for different durations from 0.5 to 4 h. As the rection time increased from 1 to 4 h, the LDPM, KN, and WSP yields progressively decreased (Fig. 6a). The decrease in the targeted product yields with increasing time can be due to repolymerization of the phenolic derivatives and holocellulose-derived intermediates (e.g., 5-HMF, FFA, LVA, and FOL) via condensation reactions, which can result in the formation of undesired phenolic resins and humins [72,73] (Fig. 6b). The MALDI–TOF/MS profiles of the DSPs collected at various reaction times confirm that the repolymerization occurred at extended periods of time (Fig. 6c). The XRD patterns of the spent catalysts that were collected after the reaction at 0.5–2 h show that the diffraction pattern intensity at $2\theta = 5$–10°, which correspond to the (101) and (020) planes of HZSM-5, decreased significantly (Zone A, Fig. 6d), while those at $2\theta = 23$–25°, which

correspond to the (051), (313), and (101) planes of HZSM-5, marginally increased as the reaction time increased (Zone B, Fig. 6d). As a result, the total crystallinity of the HZSM-5 in the 5C–5R/Z(100) catalyst decreased by 13% when the reaction time was extended from 0.5 to 2 h (Fig. 6e). HZSM-5 decrystallization could be initiated via desilication (Si–O bond hydrolysis) and dealumination (Al–O bond hydrolysis) under hydrothermal conditions [74,75].

To further examine plausible reasons for the deactivation and to explore a potential deactivation suppression approach, a catalyst reusability test was conducted at 300 °C and 3.0 MPa for 1 h with oakwood as feedstock. The spent 5C–5R/Z(100) catalyst collected after the 1st run (which was denoted as 5C–5R/Z(100)-S) was tested in the 2nd run. Prior to the next run, the spent catalyst was washed with water followed by acetone for humin and lignin-derived oligomer removal and dried overnight in a vacuum at 80 °C. The dried catalyst was calcined at 550 °C for 4 h in an air flow followed by reduction at 450 °C for 4 h in a 5% H$_2$/Ar gas flow to reactivate the catalyst. The oakwood conversion and product yield over the activated 5C–5R/Z(100)-S catalyst decreased significantly in the 2nd run (Fig. 7a). Thus, significant deactivation
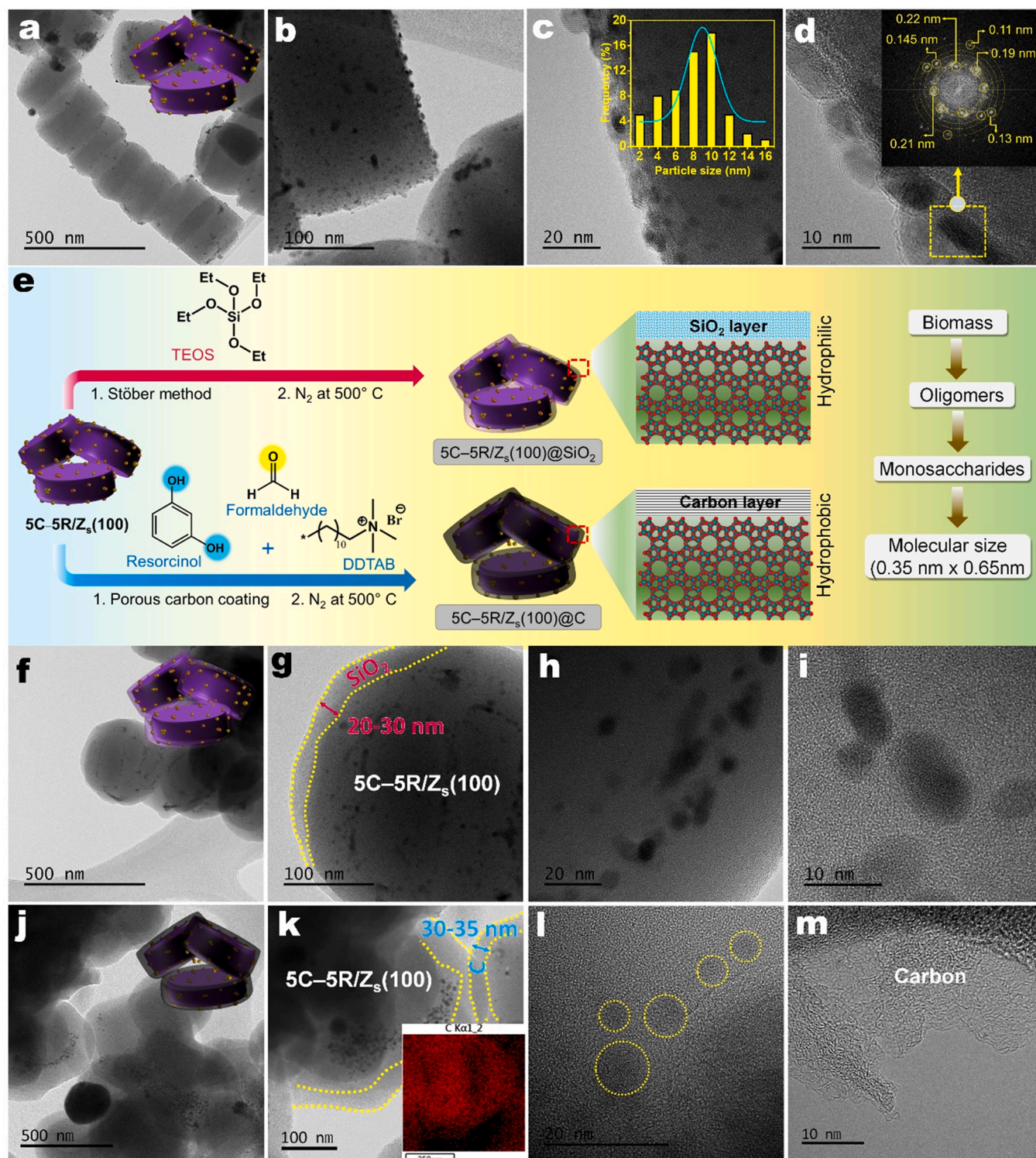
Fig. 9. (a–d) HR–TEM images of the 5C–5R/Z$_s$(100) catalyst (inset of (c): particle size distribution; inset of (d): fast Fourier-transform image). (e) Schematic for the SiO$_2$ and carbon coating on the 5C–5R/Z$_s$(100) catalyst. HR–TEM images of the (f–i) 5C–5R/Z$_s$(100)@SiO$_2$ and (j–m) 5C–5R/Z$_s$(100)@C catalysts (inset of (k): elemental mapping of carbon).

occurred during the complete biomass conversion reaction. The decrease in catalyst activity could be attributed to several factors, including poisoning via inorganic species deposition to the metal sites, structural changes of the zeolitic support, metal leaching, and coke deposition. The oakwood used in this study contained a non-negligible amount of ash (2.2 wt%, Table S2); among the ash in the oakwood, Ca, Si, and K are the major species [76]. These alkali metals can

potentially be poisonous to the metal sites [77]. In addition, the presence of alkali metals in lignocellulosic biomass could potentially facilitate the hydrolysis of Si–O–Al bridges in the zeolitic framework [78]. As shown in Fig. 7b, due to the damage in the zeolitic framework, the 5C–5R/Z(100)-S catalyst exhibited large mesopores. Mesopore formation in the 5C–5R/Z(100)-S catalyst could potentially trap high-molecular-weight carbonaceous species (e.g., humins and
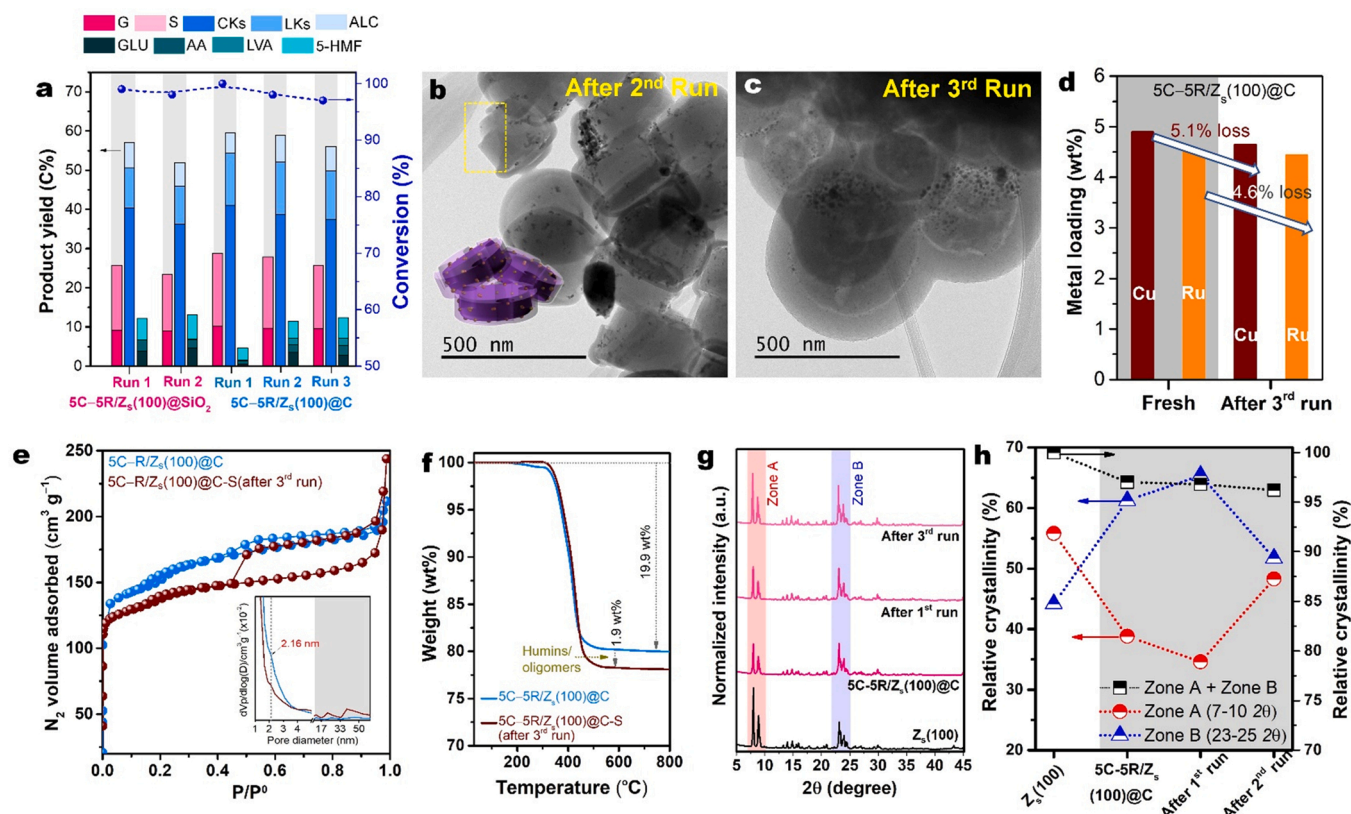
Fig. 10. (a) Reusability test results of the 5C–5R/Z$_s$(100)@SiO$_2$ and 5C–5R/Z$_s$(100)@C catalysts. HR–TEM images of the (b) spent 5C–5R/Z$_s$(100)@SiO$_2$ catalyst collected after the 2nd run and the (c) spent 5C–5R/Z$_s$(100)@C catalyst collected after the 3rd run. (d) ICP–OES data, (e) N$_2$ adsorption–desorption profiles (inset figure: pore size distribution), (f) TGA profiles, (g) XRD patterns, and (h) relative crystallinity of the fresh and spent 5C–5R/Z$_s$(100)@C catalysts. The relative crystallinity percentage ($2\theta = 5$–$35°$) was calculated as follows: RC% = I_c/I_c+I_a, where I_c and I_a are the total crystallinity of the crystalline and amorphous peaks. Reaction conditions: 0.5 g of oakwood, 30 mL of H$_2$O, a feed-to-catalyst ratio of 2, a temperature of 300 °C, an initial H$_2$ pressure of 3.0 MPa, and a duration of 1 h.

lignin-derived oligomers) during the reaction, which in turn can block the active sites. As shown in Fig. 7c, approximately 8 wt% organic species were deposited on the 5C–5R/Z(100)-S catalyst. In the H$_2$–TPR profiles shown in Fig. 7d, the reduction peaks of the 5C–5R/Z(100)-S catalyst were upshifted compared to the fresh 5C–5R/Z(100) catalyst due to metal NP agglomeration. After the 1st run, the Ru and Cu dispersion in the 5C–5R/Z(100)-S catalyst decreased by 28% and 21%, respectively (Table 1). In addition, the total amount of H$_2$ consumed significantly decreased to 44%. Moreover, approximately 22% of Cu and 28% of Ru were leached out in the 5C–5R/Z(100)-S catalyst (Fig. 7e). Thus, severe metal NP leaching and agglomeration occurred during the oakwood conversion. Furthermore, as shown in Fig. 7 f, severe structural deformation of HZSM-5 occurred in the 5C–5R/Z(100)-S catalyst, which can be caused by the desilication during the hydrothermal reaction; this could contribute to metallic site agglomeration. A schematic for the catalyst deactivation is shown in Fig. 7 g.

3.6. Strategies to enhance catalyst stability

A well-established technique to maintain catalyst activity is metal NP encapsulation, which can not only prohibit metal NP aggregation but also inhibit metal species leaching owing to the spatial conferment in the microporous topology [79]. To overcome the issues associated with metal leaching, metal NP agglomeration, and coke deposition on the metal sites, the Cu–Ru NPs were encapsulated inside the zeolitic framework. As shown in Fig. 8a–d, HR–TEM images of the 1.6C–1.5R/Z$_s$(100)-E catalyst confirm the Cu–Ru NP encapsulation inside of zeolite. Some fraction metal NPs were not trapped inside the zeolitic domain, resulting in lower metal loadings (Fig. 8e) and lower intensity of the Cu (111) and Ru (101) peaks in the XRD pattern (Fig. 1a)

compared to those of 5C–5R/Z(100). To evaluate the effect of the encapsulation on catalytic stability, three reaction cycles were carried out at 300 °C and 3.0 MPa for 1 h with oakwood as feedstock. The encapsulated 1.6C–1.5R/Z$_s$(100)-E catalyst exhibited a significantly enhanced stability compared to the 5C–5R/Z(100) catalyst (Fig. 8f). In addition, the crystallinity of the zeolite in the encapsulated catalyst was maintained after the 3rd run (Fig. 8 g). However, interparticle aggregation between neighboring zeolitic particles were observed in the spent catalysts collected after the 1st and 3rd runs (Fig. 8h–k). Overall, the encapsulated catalyst has a much better hydrothermal stability than the non-encapsulated catalyst.

Motivated by the enhanced stability of the encapsulated 1.6C–1.5R/Z$_s$(100)-E catalyst, two more strategies to increase the hydrothermal stability of the metal-supported zeolitic catalyst were examined: SiO$_2$ and carbon layer coating on the surface of the 5C–5R/Z(100) catalyst. Previously, several attempts have been made to increase the hydrothermal stability of zeolites, including silylation [80], silicalite-1 coating [81,82], and carbon coating [83]. In this study, due to the non-uniform shape and wide size distribution of the commercial Z(100) sample (Fig. 2a), it was difficult to form a uniform conformal coating on the surface of individual zeolitic supports. To address this non-uniformity issue, uniform micron-sized HZSM-5 particles were synthesized, which exhibited preferential growth along the *c*-axis direction (Fig. S19a) and were denoted as Z$_s$(100). The Z$_s$(100) exhibited a typical type-II N$_2$ adsorption–desorption isotherm with a typical hysteresis loop in the range of $0.9 < p/p^0 < 1.0$ (Fig. S19b). The textural properties and total acid sites of the Z$_s$(100) were similar to those of the commercial Z(100), as listed in Tables 1 and 2. Crystallinity of zeolite structure in 5C–5R/Z$_s$(100) catalyst (Fig. S20) was maintained after 5 wt% Cu and 5 wt% Ru loading on the Z$_s$(100) (Fig. 9a–d). Finally, the as-synthesized

5C–5R/Z$_s$(100) catalyst was used to coat with the SiO$_2$ or carbon (C) layer (Fig. 9e). The SiO$_2$ layer thickness in the 5C–5R/Z$_s$(100)@SiO$_2$ catalyst was in the range of 20–30 nm (Fig. 9f and g). In the 5C–5R/Z$_s$(100)@C catalyst case, a thin carbon layer coating with a thickness of 30–35 nm was observed (Fig. 9j and k). Cu–Ru NPs were observed under the SiO$_2$ and carbon sublayer (Fig. 9h and i and l, respectively).

To demonstrate the stability of the 5C–5R/Z$_s$(100)@SiO$_2$ and 5C–5R/Z$_s$(100)@C catalysts, the oakwood conversion was performed at a temperature of 300 °C and an initial H$_2$ pressure of 3.0 MPa for 1 h, and the results are shown in Fig. 10a. In the 1st run over the 5C–5R/Z$_s$(100)@SiO$_2$ catalyst, the LDPM and KN yields were 50.6% and 25.8%, respectively. The spent catalyst was washed with water followed by acetone and reduced at 450 °C for 4 h in a 5% H$_2$/Ar gas flow for re-activation. The LDPM and KN yields decreased to 40.5% and 23.4%, respectively, over the spent 5C–5R/Z$_s$(100)@SiO$_2$-S catalyst. One of plausible reasons for the decrease in catalyst activity is the stability of the SiO$_2$ layer coated on the catalyst surface. As shown in Fig. 10b, the SiO$_2$ layer was detached from the Z$_s$(100) surface in the spent 5C–5R/Z$_s$(100)@SiO$_2$-S catalyst. The 5C–5R/Z$_s$(100)@C catalyst exhibited higher LDPM and KN yields in the 1st run (54.3% and 28.7%, respectively) and higher stability in the 2nd run (52.1% and 27.9%, respectively) compared to the 5C–5R/Z$_s$(100)@SiO$_2$ catalyst. The LDPM and KN yields slightly decreased to 49.8% and 25.8%, respectively, over the 5C–5R/Z$_s$(100)@C-S catalyst in the 3rd run. As opposed to the SiO$_2$ layer, the carbon layer was maintained in the spent 5C–5R/Z$_s$(100)@C-S catalyst that was collected after the 3rd run (Fig. 10c). Because of the strong and conformal carbon layer coating, metal NP leaching was suppressed (Fig. 10d). Even after the carbon coating, some degree of desilication was observed to form mesopores (Fig. 10e). However, the carbon coating could suppress the deposition of high-molecular weight species (e.g., humins, lignin-derived oligomers, and cokes) on the spent 5C–5R/Z$_s$(100)@C-S catalyst that was collected after the 3rd run (Fig. 10 f). The total crystallinity of Z$_s$(100) in the fresh 5C–5R/Z$_s$(100) @C catalyst only decreased marginally by 4% in the spent fresh 5C–5R/Z$_s$(100)@C-S catalyst (Fig. 10 g and h). Therefore, the carbon-coated 5C–5R/Z$_s$(100)@C-S catalyst exhibited a significantly enhanced catalyst stability in the conversion of lignocellulosic biomass to value-added platform chemicals.

4. Conclusion

Complete lignocellulosic biomass was converted into various value-added chemicals over a multifunctional bi-metallic Cu–Ru/H-ZSM5 catalyst in an aqueous medium. The H-ZSM5 with a Si/Al ratio of 100 provided a suitable acidity for the consecutive depolymerization, dehydration, and isomerization, of holocellulose, and Cu–Ru NPs synergistically promoted hydrogenation/hydrogenolysis and stabilization of lignin-derived reactive intermediates. Direct oakwood conversion over the 5C–5R/HZSM-5(100) catalyst yielded 27 wt% cyclic ketones (e. g., cyclopentanone and its methyl derivatives), 9.1 wt% LDPMs (e.g., (propyl-substituted) guaiacols and (propyl-substituted) syringols), and 6.0 wt% linear ketones (e.g., 2,5-hexanedione and 2-pentanone) based on the total weight of feed at a temperature of 300 °C and an initial H$_2$ pressure of 3.0 MPa for 1 h. The close proximity between the Cu and Ru NPs could facilitate hydrogen spillover from the Ru domain to the Cu domain, while the Cu^{1+}/Cu^0 sites contributes on adsorption and activation of the C=O bond containing of reaction intermediate species, which could lead direct the pathways to cyclopentanones. Cu and Ru NP encapsulation inside the zeolite and carbon layer coating on the 5C–5R/HZSM-5(100) catalyst showed a promising potential to overcome the hydrothermal instability associated with zeolite. The one-pot lignocellulosic biomass conversion presented in this paper could be a promising and energy-efficient approach for the conversion of complete lignocellulosic biomass into versatile platform chemicals that can be used in the pharmaceutical, fragrance, and polymer industries.

CRediT authorship contribution statement

Gladys Tiffany Jaya: Methodology, Formal analysis, Data Curation, Writing – original draft. **Rizki Insyani:** Conceptualization, Methodology, Investigation, Data Curation. **Jaeyong Park:** Validation, Formal analysis, Data curation. **Amsalia Florence Barus:** Methodology, Validation, Formal analysis. **Malyil Gopalan Sibi:** Validation, Data curation, Visualization. **Virendra Ranaware:** Validation, Formal analysis. **Deepak Verma:** Conceptualization, Methodology, Formal analysis, Investigation, Writing – review & editing. **Jaehoon Kim:** Supervision, Project administration, Resources, Writing – review & editing, Funding acquisition.

Declaration of Competing Interest

The authors declare that they have no known competing financial interests or personal relationships that could have appeared to influence the work reported in this paper.

Acknowledgements

Appendix A. Supporting information

Supplementary data associated with this article can be found in the online version at doi:10.1016/j.apcatb.2022.121368.

References

[1] L. Lin, X. Han, B. Han, S. Yang, Emerging heterogeneous catalysts for biomass conversion: studies of the reaction mechanism, Chem. Soc. Rev. 50 (2021) 11270–11292, https://doi.org/10.1039/D1CS00039J.

[2] Y. Román-Leshkov, C.J. Barrett, Z.Y. Liu, J.A. Dumesic, Production of dimethylfuran for liquid fuels from biomass-derived carbohydrates, Nature 447 (2007) 982–985, https://doi.org/10.1038/nature05923.

[3] R. Insyani, D. Verma, H.S. Cahyadi, S.M. Kim, S.K. Kim, N. Karanwal, J. Kim, One-pot di- and polysaccharides conversion to highly selective 2,5-dimethylfuran over Cu-Pd/Amino-functionalized Zr-based metal-organic framework (UiO-66(NH2)) @SGO tandem catalyst, Appl. Catal. B: Environ. 243 (2019) 337–354, https://doi.org/10.1016/j.apcatb.2018.10.036.

[4] R. Insyani, D. Verma, S.M. Kim, J. Kim, Direct one-pot conversion of monosaccharides into high-yield 2, 5-dimethylfuran over a multifunctional Pd/Zr-based metal–organic framework@ sulfonated graphene oxide catalyst, Green. Chem. 19 (2017) 2482–2490, https://doi.org/10.1039/C7GC00269F.

[5] H.C. Ong, W.-H. Chen, A. Farooq, Y.Y. Gan, K.T. Lee, V. Ashokkumar, Catalytic thermochemical conversion of biomass for biofuel production: a comprehensive review, Renew. Sustain. Energy Rev. 113 (2019) 109266, https://doi.org/10.1016/j.rser.2019.109266.

[6] H. Jo, H. Prajitno, H. Zeb, J. Kim, Upgrading low-boiling-fraction fast pyrolysis bio-oil using supercritical alcohol: understanding alcohol participation, chemical composition, and energy efficiency, Energy Convers. Manag. 148 (2017) 197–209, https://doi.org/10.1016/j.enconman.2017.05.061.

[7] N. Karanwal, M.G. Sibi, M.K. Khan, A.A. Myint, B. Chan Ryu, J.W. Kang, J. Kim, Trimetallic Cu–Ni–Zn/H-ZSM-5 catalyst for the one-pot conversion of levulinic acid to high-yield 1, 4-pentanediol under mild conditions in an aqueous medium, ACS Catal. 11 (2021) 2846–2864, https://doi.org/10.1021/acscatal.0c04216.

[8] N. Karanwal, D. Verma, P. Butolia, S.M. Kim, J. Kim, One-pot direct conversion of levulinic acid into high-yield valeric acid over a highly stable bimetallic Nb-Cu/Zr-doped porous silica catalyst, Green. Chem. 22 (2020) 766–787, https://doi.org/10.1039/C9GC03516H.

[9] D. Verma, R. Insyani, H.S. Cahyadi, J. Park, S.M. Kim, J.M. Cho, J.W. Bae, J. Kim, Ga-doped Cu/H-nanozeolite-Y catalyst for selective hydrogenation and hydrodeoxygenation of lignin-derived chemicals, Green. Chem. 20 (2018) 3253–3270, https://doi.org/10.1039/C8GC00629F.

[10] Y. Liu, L. Chen, T. Wang, Q. Zhang, C. Wang, J. Yan, L. Ma, One-pot catalytic conversion of raw lignocellulosic biomass into gasoline alkanes and chemicals over LiTaMoO6 and ru/c in aqueous phosphoric acid, ACS Sustain. Chem. Eng. 3 (2015) 1745–1755, https://doi.org/10.1021/acssuschemeng.5b00256.

[11] B. Op de Beeck, M. Dusselier, J. Geboers, J. Holsbeek, E. Morré, S. Oswald, L. Giebeler, B.F. Sels, Direct catalytic conversion of cellulose to liquid straight-chain alkanes, Energy Environ. Sci. 8 (2015) 230–240, https://doi.org/10.1039/C4EE01523A.

[12] Q. Xia, Z. Chen, Y. Shao, X. Gong, H. Wang, X. Liu, S.F. Parker, X. Han, S. Yang, Y. Wang, Direct hydrodeoxygenation of raw woody biomass into liquid alkanes, Nat. Commun. 7 (2016) 11162, https://doi.org/10.1038/ncomms11162.

[13] C. Li, M. Zheng, A. Wang, T. Zhang, One-pot catalytic hydrocracking of raw woody biomass into chemicals over supported carbide catalysts: simultaneous conversion of cellulose, hemicellulose and lignin, Energy Environ. Sci. 5 (2012) 6383–6390, https://doi.org/10.1039/C1EE02684D.

[14] T.D. Matson, K. Barta, A.V. Iretskii, P.C. Ford, One-pot catalytic conversion of cellulose and of woody biomass solids to liquid fuels, J. Am. Chem. Soc. 133 (2011) 14090–14097, https://doi.org/10.1021/ja205436c.

[15] J. Park, H.S. Cahyadi, U. Mushtaq, D. Verma, D. Han, K.-W. Nam, S.K. Kwak, J. Kim, Highly efficient reductive catalytic fractionation of lignocellulosic biomass over extremely low-loaded Pd catalysts, ACS Catal. 10 (2020) 12487–12506, https://doi.org/10.1021/acscatal.0c03393.

[16] J. Park, A. Riaz, D. Verma, H.J. Lee, H.M. Woo, J. Kim, Fractionation of lignocellulosic biomass over core-shell Ni-alumina catalysts with formic acid as a co-catalyst and hydrogen source, ChemSusChem 12 (2019) 1743–1762, https://doi.org/10.1002/cssc.201802847.

[17] T. Renders, E. Cooreman, S. Van den Bosch, W. Schutyser, S.F. Koelewijn, T. Vangeel, A. Deneyer, G. Van den Bossche, C.M. Courtin, B.F. Sels, Catalytic lignocellulose biorefining in n-butanol/water: a one-pot approach toward phenolics, polyols, and cellulose, Green. Chem. 20 (2018) 4607–4619, https://doi.org/10.1039/C8GC01031E.

[18] M. Renz, Ketonization of carboxylic acids by decarboxylation: mechanism and scope, Eur. J. Org. Chem. 2005 (2005) 979–988, https://doi.org/10.1002/ejoc.200400546.

[19] J. Thorpe, G. Kon, Cyclopentanone, Org. Synth. 5 (2003) 37, https://doi.org/10.15227/orgsyn.005.0037.

[20] ⟨https://www.wboc.com/story/44083145/cyclopentanone-market-size-is-set-to-a nticipated-worth-191511-million-usd-globally-grow-with-a-cagr-of-866-top-count ries-data-analysis-by-trends⟩, pp.,

[21] G. Semple, P.J. Skinner, T. Gharbaoui, Y.-J. Shin, J.-K. Jung, M.C. Cherrier, P. J. Webb, S.Y. Tamura, P.D. Boatman, C.R. Sage, 3-(1H-tetrazol-5-yl)-1, 4, 5, 6-tetrahydro-cyclopentapyrazole (MK-0354): a partial agonist of the nicotinic acid receptor, G-protein coupled receptor 109a, with antilipolytic but no vasodilatory activity in mice, J. Med. Chem. 51 (2008) 5101–5108, https://doi.org/10.1021/jm800258p.

[22] J.M. Coterón, D. Catterick, J. Castro, Ma.J. Chaparro, B. Díaz, E. Fernández, S. Ferrer, F.J. Gamo, M. Gordo, J. Gut, Falcipain inhibitors: optimization studies of the 2-pyrimidinecarbonitrile lead series, J. Med. Chem. 53 (2010) 6129–6152, https://doi.org/10.1021/jm100556b.

[23] Y. Liu, R. Wang, H. Qi, X.Y. Liu, G. Li, A. Wang, X. Wang, Y. Cong, T. Zhang, N. Li, Synthesis of bio-based methylcyclopentadiene via direct hydrodeoxygenation of 3-methylcyclopent-2-enone derived from cellulose, Nat. Commun. 12 (2021) 1–7, https://doi.org/10.1038/s41467-020-20264-3.

[24] J. Guo, G. Xu, Z. Han, Y. Zhang, Y. Fu, Q. Guo, Selective conversion of furfural to cyclopentanone with CuZnAl catalysts, ACS Sustain. Chem. Eng. 2 (2014) 2259–2266, https://doi.org/10.1021/sc5003566.

[25] M. Dohade, P.L. Dhepe, Efficient method for cyclopentanone synthesis from furfural: understanding the role of solvents and solubility in a bimetallic catalytic system, Catal. Sci. Technol. 8 (2018) 5259–5269, https://doi.org/10.1039/C8CY01468J.

[26] R. Fang, H. Liu, R. Luque, Y. Li, Efficient and selective hydrogenation of biomass-derived furfural to cyclopentanone using Ru catalysts, Green. Chem. 17 (2015) 4183–4188, https://doi.org/10.1039/C5GC01462J.

[27] Y. Yang, Z. Du, Y. Huang, F. Lu, F. Wang, J. Gao, J. Xu, Conversion of furfural into cyclopentanone over Ni–Cu bimetallic catalysts, Green. Chem. 15 (2013) 1932–1940, https://doi.org/10.1039/C3GC37133F.

[28] C. Verrier, S. Moebs-Sanchez, Y. Queneau, F. Popowycz, The Piancatelli reaction and its variants: recent applications to high added-value chemicals and biomass valorization, Org. Biomol. Chem. 16 (2018) 676–687, https://doi.org/10.1039/C7OB02962D.

[29] G. Piancatelli, A. Scettri, S. Barbadoro, A useful preparation of 4-substituted 5-hydroxy-3-oxocyclopentene, Tetrahedron Lett. 17 (1976) 3555–3558, https://doi.org/10.1016/S0040-4039(00)71357-8.

[30] Y. Kobayashi, H. Katakami, E. Mine, D. Nagao, M. Konno, L.M. Liz-Marzán, Silica coating of silver nanoparticles using a modified Stöber method, J. Colloid Interf. Sci. 283 (2005) 392–396, https://doi.org/10.1016/j.jcis.2004.08.184.

[31] W. Luo, Y. Wang, S. Chou, Y. Xu, W. Li, B. Kong, S.X. Dou, H.K. Liu, J. Yang, Critical thickness of phenolic resin-based carbon interfacial layer for improving long cycling stability of silicon nanoparticle anodes, Nano Energy 27 (2016) 255–264, https://doi.org/10.1016/j.nanoen.2016.07.006.

[32] O. Hinrichsen, T. Genger, M. Muhler, Chemisorption of N2O and H2 for the surface determination of copper catalysts, Chem. Eng. Technol. 23 (2000) 956–959, https://doi.org/10.1002/1521-4125.

[33] H. Prajitno, R. Insyani, J. Park, C. Ryu, J. Kim, Non-catalytic upgrading of fast pyrolysis bio-oil in supercritical ethanol and combustion behavior of the upgraded oil, Appl. Energy 172 (2016) 12–22, https://doi.org/10.1016/j.apenergy.2016.03.093.

[34] M.T. Amiri, G.R. Dick, Y.M. Questell-Santiago, J.S. Luterbacher, Fractionation of lignocellulosic biomass to produce uncondensed aldehyde-stabilized lignin, Nat. Protoc. 14 (2019) 921–954, https://doi.org/10.1038/s41596-018-0121-7.

[35] R.F. Susanti, L.W. Dianningrum, T. Yum, Y. Kim, B.G. Lee, J. Kim, High-yield hydrogen production from glucose by supercritical water gasification without added catalyst, Int. J. Hydrog. Energy 37 (2012) 11677–11690, https://doi.org/10.1016/j.ijhydene.2012.05.087.

[36] M. Raevskaya, I. Yanson, A. Tatarkina, I. Sokolova, The effect of nickel on interaction in the copper-ruthenium system, J. Less Common Met. 132 (1987) 237–241, https://doi.org/10.1016/0022-5088(87)90579-0.

[37] H. Okamoto, Cu-Ru (copper-ruthenium), J. Phase, Equilibria 13 (1992) 440, https://doi.org/10.1007/BF02674997.

[38] J. Fu, K. Yang, C. Ma, N. Zhang, H. Gai, J. Zheng, B.H. Chen, Bimetallic Ru–Cu as a highly active, selective and stable catalyst for catalytic wet oxidation of aqueous ammonia to nitrogen, Appl. Catal. B: Environ. 184 (2016) 216–222, https://doi.org/10.1016/j.apcatb.2015.11.031.

[39] J. Kim, W. Choi, J.W. Park, C. Kim, M. Kim, H. Song, Branched copper oxide nanoparticles induce highly selective ethylene production by electrochemical carbon dioxide reduction, J. Am. Chem. Soc. 141 (2019) 6986–6994, https://doi.org/10.1021/jacs.9b00911.

[40] L. Martin, H. Martinez, D. Poinot, B. Pecquenard, F. Le Cras, Comprehensive X-ray photoelectron spectroscopy study of the conversion mechanism of CuO in lithiated thin film electrodes, J. Phys. Chem. C 117 (2013) 4421–4430, https://doi.org/10.1021/jp3119633.

[41] L.S. Kau, K.O. Hodgson, E.I. Solomon, X-ray absorption edge and EXAFS study of the copper sites in zinc oxide methanol synthesis catalysts, J. Am. Chem. Soc. 111 (1989) 7103–7109, https://doi.org/10.1021/ja00200a032.

[42] L.S. Kau, D.J. Spira-Solomon, J.E. Penner-Hahn, K.O. Hodgson, E.I. Solomon, X-ray absorption edge determination of the oxidation state and coordination number of copper. Application to the type 3 site in Rhus vernicifera laccase and its reaction with oxygen, J. Am. Chem. Soc. 109 (1987) 6433–6442, https://doi.org/10.1021/ja00255a032.

[43] R. Bulánek, B. Wichterlová, Z. Sobalík, J. Tichý, Reducibility and oxidation activity of Cu ions in zeolites: effect of Cu ion coordination and zeolite framework composition, Appl. Catal. B: Environ. 31 (2001) 13–25, https://doi.org/10.1016/S0926-3373(00)00268-X.

[44] R. Insyani, A.F. Barus, R. Gunawan, J. Park, G.T. Jaya, H.S. Cahyadi, M.G. Sibi, S. K. Kwak, D. Verma, J. Kim, RuO2–Ru/Hβ zeolite catalyst for high-yield direct conversion of xylose to tetrahydrofurfuryl alcohol, Appl. Catal. B: Environ. 291 (2021) 120120, https://doi.org/10.1016/j.apcatb.2021.120120.

[45] X. Liu, Q. Han, W. Shi, C. Zhang, E. Li, T. Zhu, Catalytic oxidation of ethyl acetate over Ru–Cu bimetallic catalysts: further insights into reaction mechanism via in situ FTIR and DFT studies, J. Catal. 369 (2019) 482–492, https://doi.org/10.1016/j.jcat.2018.11.025.

[46] Y. Wan, J. Ma, Z. Wang, W. Zhou, S. Kaliaguine, Selective catalytic reduction of NO over Cu-Al-MCM-41, J. Catal. 227 (2004) 242–252, https://doi.org/10.1016/j.jcat.2004.07.016.

[47] J.H. Kwak, J. Hu, D. Mei, C.-W. Yi, D.H. Kim, C.H. Peden, L.F. Allard, J. Szanyi, Coordinatively unsaturated Al3+ centers as binding sites for active catalyst phases of platinum on γ-Al2O3, Science 325 (2009) 1670–1673, https://doi.org/10.1126/science.1176745.

[48] W.C. Conner Jr, J.L. Falconer, Spillover in heterogeneous catalysis, Chem. Rev. 95 (1995) 759–788, https://doi.org/10.1021/cr00035a014.

[49] S. Velu, S.K. Gangwal, Synthesis of alumina supported nickel nanoparticle catalysts and evaluation of nickel metal dispersions by temperature programmed desorption, Solid State Ion. 177 (2006) 803–811, https://doi.org/10.1016/j.ssi.2006.01.031.

[50] G. Laurent, F. Martín, H. Busnengo, Theoretical study of hydrogen dissociative adsorption on strained pseudomorphic monolayers of Cu and Pd deposited onto a Ru (0001) substrate, Phys. Chem. Chem. Phys. 11 (2009) 7303–7311, https://doi.org/10.1039/B821422K.

[51] K. Hadjiivanov, Identification and characterization of surface hydroxyl groups by infrared spectroscopy, Adv. Catal. 57 (2014) 99–318, https://doi.org/10.1016/B978-0-12-800127-1.00002-3.

[52] F. Yi, F. Chen, Z. Tao, C. Hu, X. Yi, A. Zheng, X. Wen, Y. Yun, Y. Yang, Y. Li, Origin of weak Lewis acids on silanol nests in dealuminated zeolite Beta, J. Catal. 380 (2019) 204–214, https://doi.org/10.1016/j.jcat.2019.10.008.

[53] T. Zhang, J. Liu, D. Wang, Z. Zhao, Y. Wei, K. Cheng, G. Jiang, A. Duan, Selective catalytic reduction of NO with NH3 over HZSM-5-supported Fe–Cu nanocomposite catalysts: The Fe–Cu bimetallic effect, Appl. Catal. B: Environ. 148 (2014) 520–531, https://doi.org/10.1016/j.apcatb.2013.11.006.

[54] E. Parry, An infrared study of pyridine adsorbed on acidic solids. Characterization of surface acidity, J. Catal. 2 (1963) 371–379, https://doi.org/10.1016/0021-9517(63)90102-7.

[55] M.I. Zaki, M.A. Hasan, F.A. Al-Sagheer, L. Pasupulety, In situ FTIR spectra of pyridine adsorbed on SiO2–Al2O3, TiO2, ZrO2 and CeO2: general considerations for the identification of acid sites on surfaces of finely divided metal oxides, colloids and surfaces A: physicochem, Eng. Asp. 190 (2001) 261–274, https://doi.org/10.1016/S0927-7757(01)00690-2.

[56] V.S. Escribano, G. Garbarino, E. Finocchio, γ-Alumina and amorphous silica–alumina: structural features, acid sites and the role of adsorbed water, Top. Catal. 60 (2017) 1554–1564, https://doi.org/10.1007/s11244-017-0838-5.

[57] X. Li, K. Peng, X. Liu, Q. Xia, Y. Wang, Comprehensive understanding of the role of brønsted and Lewis Acid sites in glucose conversion into 5–hydroxymethylfurfural, ChemCatChem 9 (2017) 2739–2746, https://doi.org/10.1002/cctc.201601203.

[58] S. Van den Bosch, T. Renders, S. Kennis, S.F. Koelewijn, G. Van den Bossche, T. Vangeel, A. Deneyer, D. Depuydt, C.M. Courtin, J.M. Thevelein, W. Schutyser, B. F. Sels, Integrating lignin valorization and bio-ethanol production: on the role of

Ni-Al2O3 catalyst pellets during lignin-first fractionation, Green. Chem. 19 (2017) 3313–3326, https://doi.org/10.1039/C7GC01324H.

[59] T. Phongpreecha, J. Liu, D.B. Hodge, Y. Qi, Adsorption of lignin β-O-4 dimers on metal surfaces in vacuum and solvated environments, ACS Sustain. Chem. Eng. 7 (2018) 2667–2678, https://doi.org/10.1021/acssuschemeng.8b05736.

[60] D. Ren, Z. Song, L. Li, Y. Liu, F. Jin, Z. Huo, Production of 2,5-hexanedione and 3-methyl-2-cyclopenten-1-one from 5-hydroxymethylfurfural, Green. Chem. 18 (2016) 3075–3081, https://doi.org/10.1039/C5GC02493E.

[61] E.R. Sacia, M.H. Deaner, A.T. Bell, Synthesis of biomass-derived methylcyclopentane as a gasoline additive via aldol condensation/hydrodeoxygenation of 2, 5-hexanedione, Green. Chem. 17 (2015) 2393–2397, https://doi.org/10.1039/C4GC02292K.

[62] M. Hronec, K. Fulajtarová, Selective transformation of furfural to cyclopentanone, Catal. Commun. 24 (2012) 100–104, https://doi.org/10.1016/j.catcom.2012.03.020.

[63] X.-L. Li, J. Deng, J. Shi, T. Pan, C.-G. Yu, H.-J. Xu, Y. Fu, Selective conversion of furfural to cyclopentanone or cyclopentanol using different preparation methods of Cu–Co catalysts, Green. Chem. 17 (2015) 1038–1046, https://doi.org/10.1039/C4GC01601G.

[64] M. Chatterjee, T. Ishizaka, H. Kawanami, Accelerated decarbonylation of 5-hydroxymethylfurfural in compressed carbon dioxide: a facile approach, Green. Chem. 20 (2018) 2345–2355, https://doi.org/10.1039/C8GC00174J.

[65] L. Durndell, G. Zou, W. Shangguan, A. Lee, K. Wilson, Structure-reactivity relations in Ru catalysed furfural hydrogenation, ChemCatChem 11 (2019) 3927–3932, https://doi.org/10.1002/cctc.201900481.

[66] M.J. Islam, M.G. Mesa, A. Osatiashtiani, M.J. Taylor, J.C. Manayil, C.M. Parlett, M. A. Isaacs, G. Kyriakou, The effect of metal precursor on copper phase dispersion and nanoparticle formation for the catalytic transformations of furfural, Appl. Catal. B: Environ. 273 (2020), 119062, https://doi.org/10.1016/j.apcatb.2020.119062.

[67] A. Gumidyala, B. Wang, S. Crossley, Direct carbon-carbon coupling of furanics with acetic acid over Brønsted zeolites, Sci. Adv. 2 (2016), e1601072, https://doi.org/10.1126/sciadv.1601072.

[68] K. Ehara, S. Saka, Decomposition behavior of cellulose in supercritical water, subcritical water, and their combined treatments, J. Wood Sci. 51 (2005) 148–153, https://doi.org/10.1007/s10086-004-0626-2.

[69] Y. Bonita, V. Jain, F. Geng, T.P. O'Connell, W.N. Wilson, N. Rai, J.C. Hicks, Direct synthesis of furfuryl alcohol from furfural: catalytic performance of monometallic and bimetallic Mo and Ru phosphides, Catal. Sci. Technol. 9 (2019) 3656–3668, https://doi.org/10.1039/C9CY00705A.

[70] B. Seemala, C.M. Cai, C.E. Wyman, P. Christopher, Support induced control of surface composition in Cu–Ni/TiO2 catalysts enables high yield co-conversion of HMF and furfural to methylated furans, ACS Catal. 7 (2017) 4070–4082, https://doi.org/10.1021/acscatal.7b01095.

[71] C. Louis, L. Delannoy, Selective hydrogenation of polyunsaturated hydrocarbons and unsaturated aldehydes over bimetallic catalysts, Adv. Catal. 64 (2019) 1–88, https://doi.org/10.1016/bs.acat.2019.08.002.

[72] J. Long, Y. Xu, T. Wang, Z. Yuan, R. Shu, Q. Zhang, L. Ma, Efficient base-catalyzed decomposition and in situ hydrogenolysis process for lignin depolymerization and char elimination, Appl. Energy 141 (2015) 70–79, https://doi.org/10.1016/j.apenergy.2014.12.025.

[73] Y.M. Questell-Santiago, M.V. Galkin, K. Barta, J.S. Luterbacher, Stabilization strategies in biomass depolymerization using chemical functionalization, Nat. Rev. Chem. 4 (2020) 311–330, https://doi.org/10.1038/s41570-020-0187-y.

[74] K. Miyake, R. Inoue, T. Miura, M. Nakai, H. Al-Jabri, Y. Hirota, Y. Uchida, S. Tanaka, M. Miyamoto, S. Inagaki, Y. Kubota, C.Y. Kong, N. Nishiyama, Improving hydrothermal stability of acid sites in MFI type aluminosilicate zeolite (ZSM-5) by coating MFI type all silica zeolite (silicalite-1) shell layer, Micro Mesopor. Mat. 288 (2019), 109523, https://doi.org/10.1016/j.micromeso.2019.05.048.

[75] A.R. Maag, G.A. Tompsett, J. Tam, C.A. Ang, G. Azimi, A.D. Carl, X. Huang, L. J. Smith, R.L. Grimm, J.Q. Bond, ZSM-5 decrystallization and dealumination in hot liquid water, Phys. Chem. Chem. Phys. 21 (2019) 17880–17892, https://doi.org/10.1039/C9CP01490J.

[76] M. Reinmöller, M. Sieradzka, M. Laabs, M. Schreiner, A. Mlonka-Mędrala, A. Kopia, B. Meyer, A. Magdziarz, Investigation of the thermal behaviour of different biomasses and properties of their low-and high-temperature ashes, Fuel 301 (2021), 121026, https://doi.org/10.1016/j.fuel.2021.121026.

[77] S.K. Kim, J.Y. Han, S.-A. Hong, Y.-W. Lee, J. Kim, Supercritical CO2-purification of waste cooking oil for high-yield diesel-like hydrocarbons via catalytic hydrodeoxygenation, Fuel 111 (2013) 510–518, https://doi.org/10.1016/j.fuel.2013.03.080.

[78] D.W. Gardner, J. Huo, T.C. Hoff, R.L. Johnson, B.H. Shanks, J.-P. Tessonnier, Insights into the hydrothermal stability of ZSM-5 under relevant biomass conversion reaction conditions, ACS Catal. 5 (2015) 4418–4422, https://doi.org/10.1021/acscatal.5b00888.

[79] C. Gao, F. Lyu, Y. Yin, Encapsulated metal nanoparticles for catalysis, Chem. Rev. 121 (2020) 834–881, https://doi.org/10.1021/acs.chemrev.0c00237.

[80] S. Prodinger, M.A. Derewinski, A. Vjunov, S.D. Burton, I. Arslan, J.A. Lercher, Improving stability of zeolites in aqueous phase via selective removal of structural defects, J. Am. Chem. Soc. 138 (2016) 4408–4415, https://doi.org/10.1021/jacs.5b12785.

[81] M. Li, Y. Hu, Y. Fang, T. Tan, Coating mesoporous ZSM-5 by thin microporous Silicalite-1 shell: formation of core/shell structure, improved hydrothermal stability and outstanding catalytic performance, Catal. Today 339 (2020) 312–320, https://doi.org/10.1016/j.cattod.2019.02.041.

[82] K. Miyake, R. Inoue, T. Miura, M. Nakai, H. Al-Jabri, Y. Hirota, Y. Uchida, S. Tanaka, M. Miyamoto, S. Inagaki, Improving hydrothermal stability of acid sites in MFI type aluminosilicate zeolite (ZSM-5) by coating MFI type all silica zeolite (silicalite-1) shell layer, Micro Mesopor. Mat. 288 (2019), 109523, https://doi.org/10.1016/j.micromeso.2019.05.048.

[83] Y. Wang, P. Guerra, A. Zaker, A.R. Maag, G.A. Tompsett, L.J. Smith, X. Huang, J. Q. Bond, M.T. Timko, Strategies for extending zeolite stability in supercritical water using thermally stable coatings, ACS Catal. 10 (2020) 6623–6634, https://doi.org/10.1021/acscatal.0c01722.